Combined forces of hydrostatic pressure and actin polymerization drive endothelial tip cell migration and sprouting angiogenesis

Igor Kondrychyn[1], Liqun He[2], Haymar Wint[1], Christer Betsholtz[2, 3] and Li-Kun Phng[1, 4]

[1] Laboratory for Vascular Morphogenesis, RIKEN Center for Biosystems Dynamics Research, Kobe 650-0047, Japan

[2] Department of Immunology, Genetics and Pathology, Rudbeck Laboratory, Uppsala University, 75185 Uppsala, Sweden

[3] Department of Medicine Huddinge, Karolinska Institutet, 14157 Huddinge, Sweden

[4] Lead contact

* Correspondence: likun.phng@riken.jp

SUMMARY

Cell migration is a key process in the shaping and formation of tissues. During sprouting angiogenesis, endothelial tip cells invade avascular tissues by generating actomyosin-dependent forces that drive cell migration and vascular expansion. Surprisingly, ECs can still invade if actin polymerization is inhibited. In this study, we show that endothelial tip cells employ an alternative mechanism of cell migration that is dependent on Aquaporin (Aqp)-mediated water inflow and increase in hydrostatic pressure. In the zebrafish, ECs express *aqp1a.1* and *aqp8a.1* in newly formed vascular sprouts in a VEGFR2-dependent manner. Aqp1a.1 and Aqp8a.1 loss-of-function studies show an impairment in intersegmental vessels formation because of a decreased capacity of tip cells to increase their cytoplasmic volume and generate membrane protrusions, leading to delayed tip cell emergence from the dorsal aorta and slower migration. Further inhibition of actin polymerization resulted in a greater decrease in sprouting angiogenesis, indicating that ECs employ two mechanisms for robust cell migration *in vivo*. Our study thus highlights an important role of hydrostatic pressure in tissue morphogenesis.

Keywords

Endothelial cell migration, Sprouting angiogenesis, Aquaporin, Water flow, Hydostatic Pressure, Actin, Zebrafish

INTRODUCTION

The blood vascular system is a dynamic, multicellular tissue that adapts to the metabolic demands of development, growth and homeostasis by altering its pattern and morphology. Macroscopic transformation in the vascular network is achieved by microscopic changes in endothelial cell (EC) behaviours. For example, vascular expansion through sprouting angiogenesis requires the coordination of EC migration, proliferation, anastomosis, lumen formation and cell rearrangements, all of which require specific cell shape changes. At the initial phase of sprouting angiogenesis, endothelial tip cells generate numerous membrane protrusions such as filopodia and lamellipodia that drive migration and anastomosis (Figueiredo et al., 2021; Gerhardt et al., 2003; Phng et al., 2013; Sauteur et al., 2017). During tubulogenesis, apical membranes deform by generating inverse blebs to expand lumens so that blood can be transported efficiently through the blood vascular network (Gebala et al., 2016). However, following vessel perfusion, ECs become less dynamic and instead develop mechanoresistance to the deforming forces of blood pressure to maintain vessel morphology (Kondrychyn et al., 2020). EC shape is therefore dynamic and changes depending on the morphogenetic state of vascular development.

It is well established that localized remodelling of actin cytoskeleton and non-myosin II contractility are instrumental in driving cell shape changes during tissue morphogenesis (Clarke and Martin, 2021; Munjal and Lecuit, 2014; Murrell et al., 2015). More recently, there is an accumulating body of work implicating a role of water flow and the resulting increase in hydrostatic pressure as another mechanical mechanism of cell shape change (Choudhury et al., 2022; Chugh et al., 2022; Li et al., 2020). For example, in the osmotic engine model of cell migration, polarized distribution of ion channels and transporters generate an osmotic gradient that drives water inflow at the leading edge and outflow at the rear, leading to forward translocation of tumour cells in confined microenvironment (Stroka et al., 2014). Additionally, hydrostatic pressure from the extracellular environment can drive tissue morphogenesis, as demonstrated during mouse blastocyst formation (Chan et al., 2019; Dumortier et al., 2019), development of the otic vesicle in the zebrafish (Mosaliganti et al., 2019) and blood vessel lumen expansion (Gebala et al., 2016). Hydrostatic pressure can therefore generate sufficient forces to shape tissues and organs to their proper form and size during development.

We have previously discovered that EC migration persists after the inhibition of actin polymerization and in the absence of filopodia to generate new blood vessels in the zebrafish

63 (Phng et al., 2013). This observation suggests the existence of an alternative mechanism of
64 migration independent of actin polymerization. In this study, we sought to determine whether
65 hydrostatic pressure regulates EC migration during sprouting angiogenesis in the zebrafish by
66 investigating the function of Aquaporins (Aqp), which are transmembrane water channels that
67 increase water permeability of cell membranes to promote transcellular water flow (Day et al.,
68 2014; Farinas et al., 1997; Kozono et al., 2002; Preston et al., 1992). We discovered that ECs of
69 newly formed intersegmental vessels (ISV) express *aqp1a.1* and *aqp8a.1* mRNA, and observed
70 the enrichment of Aqp1a.1 and Aqp8a.1 proteins in the leading edge of migrating tip cells.
71 Detailed single cell analyses showed that endothelial tip cells lacking *aqp1a.1* and *aqp8a.1*
72 expression have reduced cell volume, membrane protrusions and migration capacity. As a result,
73 there is defective sprouting angiogenesis and ISV formation in *aqp1a.1;aqp8a.1* double mutant
74 zebrafish. Notably, when actin polymerization is inhibited in *aqp1a.1*;*aqp8a.1* double mutant
75 zebrafish, there is a greater impairment in EC migration and sprouting angiogenesis, demonstrating
76 the additive function of actin polymerization and hydrostatic pressure (that is elevated by water
77 inflow) in generating membrane protrusions to drive EC migration *in vivo*.
78
79 **RESULTS**
80
81 ***aqp1a.1* and *aqp8a.1* are differentially expressed by tip and stalk cells during sprouting**
82 **angiogenesis**
83 Of the 18 *aquaporin* genes that are expressed in zebrafish (Tingaud-Sequeira et al., 2010), *aqp1a.1*
84 and *aqp8a.1* mRNA have been detected in blood endothelial cells (ECs) (Koun et al., 2016; Rehn
85 et al., 2011). We confirmed the endothelial expression of *aqp1a.1* and *aqp8a.1* at 30 hours post
86 fertilization (hpf) and 2-, 3- and 4-days post fertilization (dpf) by whole-mount *in situ* hybridization
87 (WISH, Fig. S1). The two endothelial *aqp* genes, however, differ in spatial expression. While
88 *aqp1a.1* is widely expressed in blood vessels of the head and trunk (dorsal aorta (DA), caudal
89 artery (CA), ISVs, dorsal longitudinal anastomotic vessels (DLAV) and caudal vein plexus) at 30
90 hpf, *aqp8a.1* expression is absent in cerebral blood vessels and is restricted to the DA, CA and the
91 ventral regions of ISVs in the trunk. After 1 dpf, *aqp8a.1* expression expands to the entire ISV and
92 DLAV. Additionally, the expression of *aqp1a.1* and *aqp8a.1* gradually decreases in the DA and
93 CA so that both are absent by 4 dpf. Single cell RNA sequencing (scRNAseq) of ECs isolated at

94 24 hpf, 34 hpf and 3 dpf further confirmed the endothelial expression of *aqp1a.1* and *aqp8a.1*
95 mRNA (Fig. S2 A - F), revealed differential expression of *aqp1a.1* and *aqp8a.1* mRNA in distinct
96 endothelial clusters and highlighted higher *aqp1a.1* transcript expression in all endothelial
97 subtypes compared to *aqp8a.1* (Fig. S2 E - H).
98 We next examined the expression pattern of *aqp1a.1* and *aqp8a.1* at the beginning of
99 sprouting angiogenesis at higher resolution using RNAscope and confocal microscopy. At 20 hpf,
100 *aqp1a.1* mRNA is highly expressed in the DA with little expression in the PCV (Fig. 1A, C and
101 Fig. S3). Closer inspection uncovered heterogeneous expression in the DA, with higher expression
102 in ECs that would be specified as tip cells (Fig. 1A, C and Fig. S3B). Indeed, tip cells of newly
103 formed vascular sprouts express higher levels of *aqp1a.1* compared to adjacent ECs in the DA at
104 20 hpf (Fig. 1A – C, Fig. S3B) and the majority of ISVs (61%) display higher *aqp1a.1* expression
105 in tip cells than in trailing stalk cells at 22 hpf (Fig. 1G). *Aqp8a.1* expression is at first largely
106 absent in the DA at 20 hpf (Fig. 1B, D and Fig. S3C) but becomes detectable at 22hpf (Fig. 1E and
107 F). Interestingly, unlike *aqp1a.1*, *aqp8a.1* expression is undetectable in tip cells of emerging ISVs
108 at 20 hpf. At 22 hpf, it is expressed in 22 out of 23 tip cells analyzed with 78% of ISVs exhibiting
109 higher *aqp8a.1* mRNA expression in stalk cells than tip cells (Fig. 1G). These observations
110 highlight differential expression pattern of *aqp1a.1* and *aqp8a.1* in newly formed vascular sprouts,
111 with *aqp1a.1* expression enriched in tip cells and *aqp8a.1* expression in stalk cells.
112
113 **VEGF-VEGFR2 signalling induces the expression of *aqp1a.1* and *aqp8a.1* mRNA**
114 We next explored whether *aqp1a.1* and *aqp8a.1* expression is regulated by VEGFR2 signalling,
115 which is highly activated in tip cells during sprouting angiogenesis (Gerhardt et al., 2003;
116 Siekmann et al., 2013). To inhibit VEGFR2 activity, embryos were treated with 1 µM ki8751 from
117 20 hpf. Relative quantitative polymerase chain reaction (qPCR) experiments showed that *aqp1a.1*
118 and *aqp8a.1* mRNA expression was suppressed by 52% ($p < 0.0001$) and 17% ($p = 0.0028$),
119 respectively, after 6 hours of ki8751 treatment when compared to DMSO-treated embryos (Fig.
120 1H). These results demonstrate that VEGFR2 activity upregulates the expression of *aqp1a.1* and
121 *aqp8a.1*. To examine whether VEGFR2 activity also regulates Aquaporin expression in human
122 ECs, we treated cultured human aortic endothelial cells (HAECs) with ki8751 for 6 hours and
123 analyzed *AQP1* expression by qPCR. *AQP8* expression was not examined since it is not expressed
124 in HAECs (data not shown). Inhibition of VEGFR2 activity with 1 nM and 10 nM ki8751

125 decreased *AQP1* mRNA expression by 31% (p = 0.0023, Fig. 1I) and 40% (p = 0.1032, Fig. 1I),
126 respectively, demonstrating cross-species conservation of VEGFR2 activity in inducing *Aqp1*
127 mRNA expression.
128
129 **Aqp1a.1 and Aqp8a.1 proteins are enriched at the leading edge of migrating tip cells**
130 To gain a better understanding of where within the cell Aquaporin protein functions, we generated
131 stable *Tg(fli1ep:aqp1a.1-mEmerald)*^{rk30} and *Tg(fli1ep:aqp8a.1-mEmerald)*^{rk31} zebrafish lines in
132 which ECs express Aqp1a.1 or Aqp8a.1 tagged with mEmerald, respectively. At 25 hpf, we
133 observed an accumulation of Aqp1a.1 (Fig. 2A) and Aqp8a.1 (Fig. 2B) in mCherryCAAX-positive
134 membrane clusters in the cytoplasm and filopodia of tip cells. Notably, many of the Aqp1a.1- or
135 Aqp8a.1-positive membrane clusters are located at the migrating front of the tip cell. Time-lapse
136 imaging capturing the process of ISV formation between 24 to 30 hpf further showed sustained
137 enrichment of Aqp1a.1 and Aqp8a.1 in clusters at the front of the tip cell as well as in filopodia
138 (Fig. 2C and D, Movie S1 and S2), suggesting that Aqp1a.1 and Aqp8a.1 may promote localized
139 water flux at the migrating edge of tip cells.
140
141 **Loss of Aqp1a.1 and Aqp8a.1 function leads to defective trunk blood vessel formation**
142 We subsequently proceeded to generate zebrafish *aqp1a.1* and *aqp8a.1* mutants to investigate the
143 function of Aquaporin-mediated water flow in blood vessel development. Using CRISPR/Cas9
144 genome editing, we targeted the first exons of *aqp1a.1* and *aqp8a.1* genes. The CRISPR-
145 generating allele *aqp1a.1*^{rk28} carries a 14-bp deletion and an 8-bp insertion in the 5' end of the gene
146 leading to a premature termination codon at amino acid 76 after 1 missense amino acid (Fig. S4A-
147 B). The *aqp8a.1*^{rk29} allele carries a 4-bp deletion in the 5' end of the gene that leads to a frameshift
148 after Thr15 and premature termination codon at amino acid 73 after 58 missense amino acids (Fig.
149 S5A-B). Using whole-mount *in situ* hybridization and qPCR analysis, we demonstrated that
150 *aqp1a.1* and *aqp8a.1* mRNA expression is significantly decreased in *aqp1a.1*$^{rk28/rk28}$ (Fig. S4C-D)
151 and *aqp8a.1*$^{rk29/rk29}$ (Fig. S5C-D) zebrafish embryos, respectively, suggesting a rapid degradation
152 of mutant mRNAs and as a result, the loss of Aquaporin protein expression.
153 Although *aqp1a.1*$^{rk28/rk28}$*;aqp8a.1*$^{rk29/rk29}$ embryos look morphologically normal when
154 compared to wildtype or *aqp1a.1*$^{+/rk28}$*;aqp8a.1*$^{+/rk29}$ embryos (Fig. S8A-D), we observed defects
155 in blood vessel formation and patterning at 1 to 3 dpf. Compared to 28 hpf control embryos whose

156 ISVs have reached the dorsal roof of the neural tube and started to form the DLAV, ISVs of
157 *aqp1a.1*$^{rk28/rk28}$*;aqp8a.1*$^{rk29/rk29}$ embryos are much less developed (Fig. 3A and D) with
158 significantly reduced length (Fig. 3E and Fig. S6H and K). Single deletion of *aqp1a.1* (Fig. 3B
159 and Fig. S6F and I) or *aqp8a.1* (Fig. 3C and Fig. S6G and J) also led to defective ISV formation,
160 although the defects are less severe compared to the loss of both *aqp1a.1* and *aqp8a.1* expression.
161 Comparison of ISV length in *aqp1a.1*$^{rk28/rk28}$, *aqp8a.1*$^{rk29/rk29}$ and *aqp1a.1*$^{rk28/rk28}$*;aqp8a.1*$^{rk29/rk29}$
162 embryos shows that the loss of *aqp1a.1* leads to a greater decrease in ISV length than the loss of
163 *aqp8a.1* (Fig. 3E, Fig. S6I and J), and that the loss of both *aqp1a.1* and *aqp8a.1* results in the
164 greatest reduction. These observations indicate an additive effect of Aqp1a.1 and Aqp8a.1 function
165 in blood vessel development and implicate Aqp1a.1 as the more dominant Aquaporin protein in
166 EC function, in line with the higher expression of *aqp1a.1* mRNA in tip cells.
167 We next examined the embryos at 3 dpf, a stage when arterial ISVs (aISVs) and venous
168 (vISVs) are fully established and lumenized, connecting the DLAV to either the DA or PCV (Fig.
169 3F and G), respectively. Such fully established ISVs are significantly reduced in embryos when
170 *aqp1a.1*, *aqp8a.1* or both *aqp1a.1* and *aqp8a.1* are deleted. Instead, these embryos display an
171 increased number of aISVs and vISVs that fail to establish a connection to the DLAV, DA or PCV
172 (Fig. 3H – J). The number of incompletely formed or truncated ISVs per embryo in *aquaporin*
173 mutants was variable, between 1 to 6, 1 to 16 and 1 to 22 truncated ISVs in *aqp8a.1*$^{rk29/rk29}$,
174 *aqp1a.1*$^{rk28/rk28}$ and *aqp1a.1*$^{rk28/rk28}$*;aqp8a.1*$^{rk29/rk29}$ embryos, respectively (Fig. S6A-D). We also
175 found that truncated ISVs appear with higher frequency in the zebrafish trunk (ISV number 5 to
176 15) rather than in the tail (ISV number 16 to 27, Fig. S6E). Detailed analysis revealed that most of
177 the truncated ISVs are vISVs that are connected to the PCV but not the DLAV (Class I in Fig. 3K),
178 followed by the absence of aISV or vISV (Class II in Fig. 3K, Fig. S7A and B). A small fraction
179 of the truncated vessels are aISVs that are not connected to the DA (Class IV in Fig. 3K, Fig. S7D)
180 or DLAV (Class V in Fig. 3K, Fig. S7E), or vISVs that are not connected to the DLAV (Class VI
181 in Fig. 3K , Fig. S7F). At some regions, there is a truncated aISV that is not connected to the DA
182 and an incomplete vISV that is not connected to the DLAV (Class III in Fig. 3K, Fig. S7C).
183 As *aqp1a.1* is expressed in the brain vasculature during development (Fig. S1), we
184 examined whether cerebral vasculature is also affected in *aqp1a.1*$^{rk28/rk28}$ embryos. At 4 dpf, we
185 found that the length of the dorsal longitudinal vein (DLV), a main blood vessel that supplies blood
186 to the choroid plexus (Bill and Korzh, 2014) was reduced in *aqp1a.1*$^{rk28/rk28}$ embryos (p = 0.0098,

187 Fig. S9A, B and E). Also, in 2 out of 21 *aqp1a.1*$^{rk28/rk28}$ embryos, the DLV was undeveloped (Fig.
188 S9C, D and F), a defect that is also observed in 50% of *vegfab*$^{-/-}$ and *vegfc*$^{-/-}$ mutant zebrafish
189 (Parab et al., 2021).
190 In summary, our analyses show that in the absence of Aqp1a.1 and/or Aqp8a.1 function,
191 there is an initial delay in ISV formation during primary sprouting angiogenesis. By 3 dpf, some
192 ISVs are completely formed (Fig. S8K and M), connecting the DA or PCV to the DLAV. However,
193 the number of completely formed ISVs is significantly decreased, with the loss of Aqp1a.1 having
194 a more severe impact compared to the loss of Aqp8a.1, and the combined loss of Aqp1a.1 or
195 Aqp8a.1 having a greater deleterious effect.
196
197 **Aquaporins promote endothelial tip cell protrusion and migration**
198 To gain a better understanding of why ISVs do not develop normally, we assessed EC number. By
199 counting the number of nuclei in aISVs and vISVs, we found a significant reduction in EC number
200 per vessel in 2 and 3 dpf *aqp1a.1*$^{rk28/rk28}$*;aqp8a.1*$^{rk29/rk29}$ embryos when compared to wildtype
201 embryos (Fig. S10A and B), suggesting that the defective formation of ISVs may result from
202 insufficient EC number. Quantification of endothelial mitotic events between 21 and 30 hpf shows
203 that there is a similar number of tip and stalk cell division in *aqp1a.1*$^{+/rk28}$*;aqp8a.1*$^{+/rk29}$ embryos
204 and *aqp1a.1*$^{rk28/rk28}$*;aqp8a.1*$^{rk29/rk29}$ embryos (Fig. S10C), indicating that decreased EC division is
205 not the cause of reduced EC number in ISVs. We next explored whether EC migration from the
206 DA is impaired by examining tip cell behaviour from 21 – 22hpf, when sprouting angiogenesis
207 begins. In *aqp1a.1*$^{+/rk28}$*;aqp8a.1*$^{+/rk29}$ embryos, tip cells emerge from the DA between 20 and 24
208 hpf (Fig. 4A) and migrate dorsally between the somite boundaries over the notochord and neural
209 tube to form primary ISVs (Fig. 4B, Movie S3). However, in *aqp1a.1*$^{rk28/rk28}$*;aqp8a.1*$^{rk29/rk29}$
210 embryos, tip cell nuclei emerge between 22 and 28 hpf (Fig. 4A). Furthermore, in some
211 *aqp1a.1*$^{rk28/rk28}$*;aqp8a.1*$^{rk29/rk29}$ embryos, tip cell membrane protrusions do not extend dorsally in
212 the direction of migration but retract back to the DA so that a primary ISV does not form at this
213 location (Fig. 4C, Movie S4), potentially giving rise to the Class II phenotype at 3 dpf (Fig. 3K
214 and Fig. S7B). These observations indicate that tip cell protrusion from the DA is significantly
215 delayed in the absence of Aqp1a.1 and Aqp8a.1 function.
216 We have previously demonstrated that filopodia facilitate EC migration by serving as a
217 template for lamellipodia formation (Phng et al., 2013). Lamellipodia frequently emanate laterally

218 from stable filopodia at the leading edge of tip cells, leading to rapid expansion of the filopodium,
219 increase in volume and the formation of a stable protrusion in the direction of migration (Phng et
220 al., 2013). This was similarly observed in *aqp1a.1*$^{+/rk28}$*;aqp8a.1*$^{+/rk29}$ embryos (Fig. 4D and Movie
221 S5) but not in *aqp1a.1*$^{rk28/rk28}$*;aqp8a.1*$^{rk29/rk29}$ embryos (Fig. 4E and Movie S6). Comparison of
222 filopodia dynamics in wildtype (Fig. 4F), *aqp1a.1*$^{+/rk28}$*;aqp8a.1*$^{+/rk29}$ and
223 *aqp1a.1*$^{rk28/rk28}$*;aqp8a.1*$^{rk29/rk29}$ (Fig. 4G) embryos revealed a significant reduction in filopodia
224 number (wildtype, 18.73 ± 5.1/100µm; *aqp1a.1*$^{+/rk28}$*;aqp8a.1*$^{+/rk29}$, 20.4 ± 6.5/100µm;
225 *aqp1a.1*$^{rk28/rk28}$*;aqp8a.1*$^{rk29/rk29}$, 9.8 ± 5.5/100µm; Fig. 4H) and length (wildtype, 5.5 ± 2.8 µm;
226 *aqp1a.1*$^{+/rk28}$*;aqp8a.1*$^{+/rk29}$, 6.0 ± 3.4 µm; *aqp1a.1*$^{rk28/rk28}$*;aqp8a.1*$^{rk29/rk29}$, 4.5 ± 2.2 µm; Fig. 4I) in
227 ECs lacking both Aqp1a.1 and Aqp8a.1 function that can be accounted for by a decrease in actin
228 polymerization (Fig. 4J). By tracking Lifeact-mCherry signal in filopodia, we determined that the
229 average elongation rate of actin as 0.055 ± 0.013 µm per second in wildtype embryos and that this
230 is significantly decreased by 47% to 0.029 ± 0.011 µm per second ($p < 0.0001$) in
231 *aqp1a.1*$^{rk28/rk28}$*;aqp8a.1*$^{rk29/rk29}$ embryos. Analysis of time-lapse images of tip cell behaviour
232 further showed slower tip cell membrane expansion at the leading edge (Fig. 4K), decreased nuclei
233 displacement (Fig. 4L) and a significant reduction in tip cell migration velocity (Fig. 4M) in
234 *aqp1a.1*$^{rk28/rk28}$*;aqp8a.1*$^{rk29/rk29}$ embryos. To determine whether the slower EC migration is caused
235 by a loss of front-rear polarity, we examined Golgi position relative to the nucleus in wildtype,
236 *aqp1a.1*$^{rk28/rk28}$ and *aqp8a.1*$^{rk29/rk29}$ embryos at 24 - 26 hpf (Fig. S10D). This analysis shows that
237 tip cell polarity is unperturbed in the absence of Aqp1a.1 or Aqp8a.1 function.
238 In conclusion, our findings demonstrate that Aqp1a.1 and Aqp8a.1 regulate sprouting
239 angiogenesis by promoting endothelial tip cell emergence from the DA, the formation and
240 expansion of membrane protrusions and EC migration.
241
242 **Tip cell volume regulation depends on Aquaporin-mediated water influx**
243 Aquaporin channels permit bidirectional flow of water across the plasma membrane, with the
244 direction of flow determined by the osmotic gradient between the extracellular environment and
245 cell cytoplasm (Agre et al., 2002). We next sought to determine whether water flows in or out of
246 tip cells during sprouting angiogenesis. We hypothesize that water flux across the cell membrane
247 can lead to changes in tip cell volume, with water influx increasing the volume while outflow
248 decreases. To quantify tip cell volume in the absence of Aquaporin function, we injected a plasmid

249 encoding *kdrl:mEmerald* into 1-cell stage *aqp1a.1*$^{rk28/rk28}$*;aqp8a.1*$^{rk29/rk29}$ embryos to label ECs in
250 a mosaic manner. We also investigated the effects of increasing Aqp1a.1 expression on tip cell
251 volume by injecting a plasmid encoding *Aqp1a.1-P2A-EGFP* into wildtype embryos. As control,
252 wildtype embryos were injected with the plasmid encoding *kdrl:mEmerald*. mEmerald/EGFP-
253 positive tip cells were imaged and their volume measured at 24 to 25 hpf from 3D reconstructions
254 of labelled cells. Wildtype ECs are on average 964.6 ± 270.2 μm^3 in size (Fig. 5A and D). In the
255 absence of both Aqp1a.1 and Aqp8a.1 function (Fig. 5B), tip cell volume significantly decreased
256 by 26% to 709.8 ± 293.5 μm^3 (p = 0.015, Fig. 5D) when compared to wildtype tip cells. The
257 overexpression of Aqp1a.1 increased tip cell volume by 36% to 1313 ± 527.4 μm^3 when compared
258 to wildtype tip cells (Fig. 5C and D, p = 0.0069) and by 85% when compared to
259 *aqp1a.1*$^{rk28/rk28}$*;aqp8a.1*$^{rk29/rk29}$ tip cells ($p < 0.0001$). These results therefore support water influx
260 as the direction of water flow in tip cells during migration, and that this is mediated through
261 Aqp1a.1 and Aqp8a.1.
262 In summary, our results demonstrate a role of endothelial Aquaporins in promoting water
263 influx to increase endothelial tip cell volume and cytoplasmic hydrostatic pressure, as well as
264 accelerate actin polymerization in filopodia (Fig. 4J).
265
266 **The anion channel, SWELL1, promotes EC migration and sprouting angiogenesis**
267 As the direction of water flow is dictated by an osmotic gradient, with water flowing from low to
268 high osmolarity, we next examined the function of ion channels in establishing an osmotic gradient.
269 SWELL1, or LRRC8A, is a component of volume-regulated anion channel (VRAC) that mediates
270 ions, especially chloride anions, and osmolyte efflux (Qiu et al., 2014; Voss et al., 2014). Recently,
271 SWELL1 has been demonstrated to polarize at the trailing edge of migrating breast cancer cells to
272 direct water efflux and confer confined migration direction (Zhang et al., 2022). In the zebrafish,
273 scRNAseq data shows that the gene encoding SWELL1, *lrrc8aa*, is expressed in a subset of ECs,
274 with 12.32% of ECs coexpressing *lrrc8aa* and *aqp1a.1* (Fig. 6A) and 10.16% coexpressing *lrrc8aa*
275 and *aqp8a.1* (Fig. 6B). To determine whether *lrrc8aa* is expressed in endothelial tip cells, we
276 performed RNAscope and confocal microscopy. Although *lrrc8aa* is expressed in surrounding
277 somites and notochord (Fig. 6C), we could also detect its expression in endothelial tip cells (Fig.
278 6D and E), suggesting that SWELL1 can establish an osmotic gradient in the vicinity of the
279 developing ISVs and within tip cells to direct water flow. To address the function of SWELL1-

280 generated osmotic gradient, we disrupted its activity by treating zebrafish with 5μM DCPIB
281 (Gunasekar et al., 2022) for 6 hours from 20 hpf and observed a similar impairment in ISV
282 formation (Fig. 6F and G) as in *aqp1a.1*$^{rk28/rk28}$*;aqp8a.1*$^{rk29/rk29}$ embryos (Fig. 3D and E). SWELL1
283 inhibition resulted in shorter ISVs formed at 26 to 27 hpf (Fig. 6H) due to impaired leading edge
284 displacement of tip cells (Fig. 6I) and decreased tip cell velocity (Fig. 6J). Further analysis of tip
285 cell morphology showed a decrease in the number (Fig. 6K) and length (Fig. 6L) of filopodia
286 formed and compromised elongation of tip cells (Fig. 6M and N, Movie S7) in DCPIB-treated
287 embryos. In summary, these results suggest that chloride efflux through SWELL1 establishes an
288 osmotic gradient, either within ECs or between EC and the surrounding interstitial tissue, to direct
289 water flow and thereby modulate EC migration and sprouting angiogenesis.
290

291 **Additive effects of actin polymerization and water influx in driving EC migration and**
292 **sprouting angiogenesis**

293 We have previously observed that ECs are still able to migrate and form ISVs after the inhibition
294 of actin polymerization (Phng et al., 2013). In these experiments, embryos were treated with a low
295 concentration of Latrunculin B (Lat. B), an inhibitor of actin polymerization, that resulted in the
296 suppression of filopodia formation. Under such conditions, ECs can generate small membrane
297 protrusions and migrate in a directed manner at a reduced speed. How ECs are still able to migrate
298 after the inhibition of actin polymerization was unclear. As our current study demonstrates a role
299 of water inflow and hydrostatic pressure as another mechanism of cell migration, we hypothesize
300 that ECs employ water influx to migrate when actin polymerization is compromised and that the
301 depletion of both water influx and actin polymerization will result in a greater inhibition of EC
302 migration.

303 To test this hypothesis, we examined ISV development in embryos with decreased actin
304 polymerization and water inflow by treating *aqp1a.1*$^{rk28/rk28}$*;aqp8a.1*$^{rk29/rk29}$ embryos with Lat. B.
305 At 28 hpf, ISVs of wildtype embryos treated with DMSO have reached the dorsal roof of the neural
306 tube (Fig. 7A) and show an average length of 104.1 ± 13.47 μm (Fig. 7E). The treatment of
307 wildtype embryos with 0.08 μg/ml Lat. B from 20 to 28 hpf (Fig. 7B) resulted in a significant
308 decrease in ISV length (61.53 ± 23.27 μm) compared to control embryos ($p < 0.0001$, Fig. 7E). A
309 similar decrease in ISV length was also observed in *aqp1a.1*$^{rk28/rk28}$*;aqp8a.1*$^{rk29/rk29}$ embryos treated
310 with DMSO (63.75 ± 30.24 μm, Fig. 7C and E). When *aqp1a.1*$^{rk28/rk28}$*;aqp8a.1*$^{rk29/rk29}$ embryos

311 were treated with 0.08μg/ml Lat. B from 20 to 28 hpf, there was a greater decrease in the length
312 of ISV formed at 28 hpf (43.10 ± 24.42 μm, Fig. 7D and E) when compared to the inhibition of
313 actin polymerization (p = 0.0028) or depletion of water influx (p < 0.0001) alone (Movie S8).
314 These results therefore demonstrate additive functions of actin polymerization and water influx in
315 driving EC migration during sprouting angiogenesis (Fig. 7F).
316
317 **DISCUSSION**
318 In this study, we demonstrate that endothelial tip cells utilize two mechanisms of migration
319 concurrently – actin polymerization and hydrostatic pressure - during sprouting angiogenesis in
320 the zebrafish. The increase in hydrostatic pressure in endothelial tip cells is generated by Aqp1a.1-
321 and Aqp8a.1-mediated water inflow. By performing detailed expression analyses, we showed that
322 *aqp1a.1* and *aqp8a.1* are differentially expressed in newly formed vascular sprouts. *Aqp1a.1* is
323 expressed earlier in the DA than *aqp8a.1* during development and in ECs destined to be tip cells.
324 In newly formed ISVs, endothelial tip cells express higher *aqp1a.1* mRNA levels while stalk cells
325 express higher *aqp8a.1* mRNA levels. In zebrafish harbouring mutations in both *aqp1a.1* and
326 *aqp8a.1*, there is delayed tip cell protrusion from the DA, decreased tip cell migration and
327 increased occurrence of truncated ISVs at 3 dpf. We further discovered that *aqp1a.1* and *aqp8a.1*
328 expression is upregulated by VEGFR2 activity, suggesting that VEGFA-VEGFR2 signalling
329 employs Aquaporin function as one mechanism to drive sprouting angiogenesis.
330 Several lines of evidence implicate Aquaporins in facilitating water flow into endothelial
331 tip cells during sprouting angiogenesis. First, timelapse imaging showed polarized localization of
332 Aqp1a.1 and Aqp8a.1 proteins at the leading edge of migrating tip cells, suggesting that water flow
333 occurs locally at the migrating front of the cell. Secondly, single cell analyses revealed Aqp1a.1-
334 and Aqp8a.1-deficient tip cells have reduced cell volume, impaired expansion of cell membranes
335 at the leading edge and decreased generation of stable cell protrusions. These observations
336 implicate water flow into tip cells, leading to increased cell volume. This is confirmed by the
337 overexpression of Aqp1a.1 in tip cells that resulted in increased cell volume. Due to the
338 incompressible property of water within an enclosed compartment such as the cell, water influx
339 will lead to elevation in hydrostatic pressure. At the leading edge of tip cells, increased hydrostatic
340 pressure would expand and deform membranes to generate protrusions. Additionally, water influx
341 can reduce cytoplasmic viscosity and increase spacing between the plasma membrane and the

342 underlying actin cytoskeleton, promoting actin monomer diffusion, actin polymerization and the
343 generation of membrane protrusions to facilitate cell migration (Boer et al., 2023; Loitto et al.,
344 2009).

345 A key finding in this study is the demonstration that endothelial tip cells employ hydrostatic
346 pressure as a second mechanism of cell migration *in vivo*. In a previous study, we discovered that
347 ECs continue to migrate when actin polymerization is inhibited and in the absence of filopodia
348 (Phng et al., 2013). Here, we show that hydrostatic pressure can generate force for EC migration
349 in the absence of actin-based force generation. When both mechanisms are perturbed, there is a
350 greater impairment in EC migration (Fig. 7D and E). This finding highlights the importance of
351 hydrostatic pressure as an additional mechanism that reinforces actin-based cell shape changes and
352 motility to ensure robust migration and formation of new blood vessels in complex three-
353 dimensional environments. Such dual mode migration is advantageous when blood vessels
354 develop in physically confined spaces such as in the zebrafish trunk, where ECs must emerge from
355 the DA and migrate between somite boundaries and over tissues such as the notochord and neural
356 tube to form ISVs. Such dependence on water flow in cell migration under confined
357 microenvironment has been reported in human MDA-MB-231 breast cancer cells and mouse S180
358 sarcoma cells, which show cell migration persistence in narrow channels after inhibition of actin
359 polymerization or myosin II-mediated contractility (Stroka et al., 2014). In this context, AQP5
360 mediates water flow and the decrease or increase in AQP5 expression suppresses or enhances,
361 respectively, cancer cell migration (Chae et al., 2008; Jung et al., 2011; Stroka et al., 2014).

362 Our findings on the endothelial function of zebrafish Aqp1a.1, which is homologous to
363 mammalian AQP1, corroborate previous studies demonstrating a function of AQP1 in promoting
364 cell migration. In tumour bearing AQP1-null mice, there is reduced tumour angiogenesis and
365 AQP1-deficient ECs display reduced migration in an *in vitro* wound healing assay (Maltaneri et
366 al., 2020; Saadoun et al., 2005). In chick, AQP1 expression levels affect neural crest cell migration
367 speed and direction by regulating filopodia length and stability (McLennan et al., 2019). The
368 regulation of membrane protrusions has also been demonstrated for other Aquaporin proteins. For
369 example, AQP9 weakens membrane-cytoskeleton anchorage and promote formation of membrane
370 protrusions such as filopodia and blebs (Karlsson et al., 2013; Loitto et al., 2007). We also
371 demonstrate for the first time a role of Aqp8a.1 in promoting EC migration and sprouting
372 angiogenesis in the zebrafish. However, its mammalian ortholog, AQP8, was shown to inhibit

373 colorectal cancer cell lines *in vitro* (Wu et al., 2017), suggesting cell- and context-dependent
374 function of AQP8 in the regulation of cell migration. The role of Aqp1a.1 and Aqp8a.1 has also
375 been recently investigated in the zebrafish. However, the authors did not report defects in EC
376 migration but instead observed altered ISV diameter in Aqp1a.1 and Aqp8a.1 knockout and
377 overexpression experiments (Chen et al., 2024). While we corroborate a decrease in the diameter
378 of aISVs and vISVs in *aqp1a.1*$^{rk28/rk28}$ and *aqp1a.1*$^{rk28/rk28}$*;aqp8a.1*$^{rk29/rk29}$ zebrafish, we observed
379 a slight increase in the diameter in *aqp8a.1*$^{rk29/rk29}$ zebrafish at 2 dpf (Fig. S11A). Furthermore,
380 unlike described in Chen et al, we could not detect a difference in ISV diameter between control
381 and Aqp1a.1- or Aqp8a.1-overexpressing ECs (Fig. S11B). The disparity in phenotypes observed
382 between our groups are likely a result of differences in the *aqp1a.1* and *aqp8a.1* mutations and the
383 level of Aqp1a.1 or Aqp8a. overexpression generated in our respective zebrafish lines.
384 A central determinant of water movement is the osmotic gradient across the membrane,
385 with water flowing in the direction of higher osmotic concentration to build up hydrostatic pressure.
386 Given a crucial role of water flow in regulating cell volume, shape and migration, it is also
387 important to understand the function and distribution of ion channels, exchangers and transporters
388 and water channels that generate an osmotic gradient across the cell. This is reflected in a growing
389 number of studies demonstrating a role of ion transporters in cell migration. In neutrophils, the
390 increase in cell volume and potentiation of cell migration depend on the sodium-proton exchanger
391 1 (NHE1) and the chloride-bicarbonate exchanger 2 (AE2) (Nagy et al., 2023). In T cells,
392 chemokine-induced migration depends on ion influx via SLC12A1, and water influx via AQP3
393 (Boer et al., 2023). In tumour cells migrating in narrow channels, the establishment of a polarized
394 distribution of Na^+/H^+ pumps and Aquaporin proteins in cell membranes is required for net inflow
395 of ions and water at the leading edge and net outflow at the trailing edge (Stroka et al., 2014).
396 Although our study identifies a function of Aqp1a.1 and Aqp8a.1 in facilitating water inflow, it
397 remains unknown which ion channels and transporters control ion flux across the cell membrane
398 to modulate water flow in tip cells. Results from our study suggest a role of SWELL1 in generating
399 an osmotic gradient that controls EC migration, since its inhibition resulted in reduced membrane
400 protrusions, slower tip cell migration and defective sprouting angiogenesis. Due to the limitations
401 of our experimental approach, we do not know whether the effect of inhibiting SWELL1 function
402 is cell autonomous or a consequence of altered chloride flux in the neighbouring cells that would
403 alter tissue osmolarity. It also remains to be clarified where SWELL1 is localized within migrating

404 ECs, how it regulates the osmotic gradient within the EC (cellular) and between the EC and the
405 surrounding interstitial tissue (extracellular) to control the direction of water flow, and whether
406 other ion channels also work in concert to modulate overall cellular and extracellular osmolarity
407 to direct EC migration.

408 We have also observed enrichment of Aqp1a.1 and Aqp8a.1 proteins in specific
409 compartments of ECs, at the leading edge of migrating endothelial tip cells as well as apical
410 membranes during lumen formation (not shown). This leads to the question of how Aquaporin
411 localization is regulated as this will determine the site of increased water inflow and hydrostatic
412 pressure. It has been shown that rapid changes in subcellular localization of mammalian
413 Aquaporins upon stimulation occurs mainly via trafficking to and from the plasma membrane
414 (Markou et al., 2022) to modulate the amount of protein in the plasma membrane. The regulation
415 of AQP subcellular relocalization via calmodulin- and/or phosphorylation-dependent mechanisms
416 has been implicated for AQP0-5 and AQP7-9 (Markou et al., 2022). For example, rapid
417 translocation of AQP1 to plasma membrane upon a hypotonic stimulus is dependent on calmodulin
418 activation and phosphorylation by protein kinases C (PKC) (Conner et al., 2012) and subcellular
419 localization of AQP8 in hepatocytes is also regulated by PKA and PI3K signalling (Gradilone et
420 al., 2005, 2003). Further work is needed to elucidate the mechanism of Aqp1a.1 and Aqp8a.1
421 protein distribution in ECs.

422 In this study, we have assumed that Aqp1a.1 and Aqp8a.1 regulate EC behaviours through
423 their ability to control water permeation based on previous studies demonstrating that water
424 molecules flow through mammalian AQP1 (Preston et al., 1992; Zeidel et al., 1992) and AQP8
425 (Liu et al., 2006; Ma et al., 1997) as well as through zebrafish orthologs Aqp1a.1 and Aqp8a.1
426 (Tingaud-Sequeira et al., 2010). However, AQP1 and AQP8 are not water-specific channels.
427 AQP1 can conduct unpolar gases such as carbon dioxide (Nakhoul et al., 1998; Prasad et al., 1998;
428 Wang et al., 2007) and nitric oxide (Herrera et al., 2006; Herrera and Garvin, 2007), and in
429 zebrafish, Aqp1a.1 also mediates the transfer for small gaseous molecules such as carbon dioxide
430 and ammonia (Talbot et al., 2015). AQP8 is permeable to ammonia (Jahn et al., 2004; Liu et al.,
431 2006) and is present in the inner mitochondrial membrane (Calamita et al., 2005), where it is
432 suggested to mediate ammonia transport rather than water fluxes (Soria et al., 2010). Nevertheless,
433 because water movement flows up an osmotic gradient, increased entry of ions into the cell through
434 Aquaporins will also trigger water inflow.

435 In summary, our study highlights the role of water influx and hydrostatic pressure as
436 another force-generating mechanism utilized by cells to build tissues during animal development.
437 We demonstrate that endothelial tip cells employ both actin polymerization and hydrostatic
438 pressure for robust sprouting angiogenesis. As morphogenetic events are governed by a
439 coordination of cell shape changes, cell migration and rearrangements, we envision that the
440 shaping and formation of other tissues will also depend on Aquaporin function and changes in
441 hydrostatic pressure.
442
443 **METHODS**
444
445 **Zebrafish maintenance and stocks.**
446 Zebrafish (*Danio rerio*) were raised and staged according to established protocols (Kimmel et al.,
447 1995). Transgenic lines used in this work are *Tg(kdrl:EGFP)*^{s843} (Jin et al., 2005), *Tg(fli1a:H2B-*
448 *EGFP)*^{ncv69} [re-named in ZFIN as *Tg(fli1:zgc:114046-EGFP)*] (Ando et al., 2019), *Tg(fli1:Lifeact-*
449 *mCherry)*^{ncv7} (Wakayama et al., 2015), *Tg(fli1:myr-mCherry)*^{ncv1} (Fukuhara et al., 2014),
450 *Tg(fli1ep:EGFP-PLC1δPH)*^{rk26} (Kondrychyn et al., 2020), *Tg(fli1:h2bc1-mCherry)*^{ncv31}
451 (Nakajima et al., 2017), *Tg(kdrl:ras-mCherry)*^{s916} (Hogan et al., 2009), *Tg(kdrl:nls-*
452 *EGFP)*^{ubs1}*;(fli1:Has.B4GALT1-mCherry)*^{bns9} (Kwon et al., 2016), *Tg(fli1ep:GAL4FF)*^{ubs2}
453 (Herwig et al., 2011). Zebrafish were maintained on a 12-hour light/12-hour dark cycle, and
454 fertilized eggs were collected and raised in E3 medium at 28^{0}C. To inhibit pigmentation in embryos
455 older than 24 hpf, 0.003% *N*-Phenylthiourea (Sigma-Aldrich) in E3 medium was used. All animal
456 experiments were approved by the Institutional Animal Care and Use Committee at RIKEN Kobe
457 Branch (IACUC).
458
459 **Plasmid construction and transgenesis.**
460 Plasmid *mEmerald-N1* was a gift from Michael Davidson (Addgene plasmid #53976), plasmids
461 *pMDS6* containing terminal *cis*-required sequences of the *Ds* transposon from maize and *pAc-SP6*
462 containing an ORF of *Ac* transposase were a gift from Sergei Parinov. Other plasmids used in this
463 study were generated by using In-Fusion HD Cloning kit (Takara Bio Inc.). A detailed information
464 regarding plasmids and primers used in this study can be found in Supplementary Tables 1 and 2,
465 respectively. *Tg(fli1ep:aqp1a.1-mEmerald)*^{rk30} and *Tg(fli1ep:aqp8a.1-mEmerald)*^{rk31} transgenic

466 zebrafish were generated by injecting *Tol2*-based *fli1ep:aqp1a.1-mEmerald* or *fli1ep:aqp8a.1-*
467 *mEmerald* plasmids (10 ng/µl), respectively, along with *Tol2 transposase* mRNA (100 ng/µl) into
468 one-cell stage AB embryos. *Tol2* transposase mRNA was transcribed from Not*I*-linearized *pCS-*
469 *TP* plasmid (a gift from Koichi Kawakami, National Institute of Genetics, Japan) using the
470 mMESSAGE mMACHINE SP6 kit (Invitrogen). Injected embryos were raised to adult and
471 screened for founders.
472
473 **Cloning of *aqp1a.1* and *aqp8a.1* genes.**
474 Total RNA was isolated from 1-day old zebrafish embryos with TRI Reagent using Direct-zol™
475 RNA MicroPrep kit (Zymo Research) according to the manufacturer's protocol. The first-strand
476 cDNA was synthesized from 1 µg of a total RNA by oligo(dT) priming using the SuperScript III
477 First-Strand synthesis system (Invitrogen) according to the manufacturer's protocol. Amplification
478 of cDNAs was performed using a high-fidelity KOD-Plus-Neo DNA polymerase (Toyobo, Japan)
479 and resulting PCR products were cloned using NEB® PCR Cloning kit (New England BioLabs).
480 Positive clones and plasmids were verified by DNA sequencing.
481
482 **Mosaic expression of DNA constructs.**
483 To avoid unnecessary *Tol2* re-transposition from the donor site in transgenic zebrafish lines
484 generated using *Tol2* transposon (Kondrychyn et al., 2009), *Ac*/*Ds* transposon system from maize
485 (Emelyanov et al., 2006) was used for mosaic expression of DNA constructs. *Ds*-based plasmids
486 (10 pg) were co-injected with 100 pg of *Ac* transposase mRNA, transcribed from Bam*HI*-
487 linearized *pAc-SP6* plasmid using the mMESSAGE mMACHINE SP6 kit (Invitrogen), into one-
488 cell stage zebrafish wildtype or *aquaporin* mutant embryos. Embryos were analyzed at 25-26 hpf
489 after injections.
490
491 ***In vivo* cell volume analysis.**
492 Single-cell labelling of ECs in ISVs was achieved by mosaic expression of *pDs-kdrl:mEmerald*
493 plasmid in wild type or *aqp1a.1*$^{rk28/rk28}$*;aqp8a.1*$^{rk29/rk29}$ mutant *Tg(fli1:Lifeact-mCherry)*^{ncv7}
494 transgenic embryos. To visualize single ECs with Aqp1a.1 overexpression, we injected *pDs-*
495 *6xUAS:aqp1a.1-P2A-EGFP-T2A-mKate2-CAAX* plasmid into *Tg(fli1:GAL4FF)*^{ubs2}*; Tg(fli1:myr-*
496 *mCherry)*^{ncv1} embryos. Embryos were imaged at 25-26 hpf with an Olympus UPLSAPO 60x/NA

497 1.2 water immersion objective with optical Z planes interval of 0.26 µm. Cell volume was
498 measured with Huygens Essential 22.10 software (Scientific Volume Imaging B.V.) using object
499 analyzer tool with manual adjustment of threshold.
500
501 **Generation of zebrafish *aqp1a.1* and *aqp8a.1* mutants.**
502 Aquaporins mutants were generated by CRISPR/Cas9-mediated mutagenesis. Guide RNAs
503 (gRNAs) targeting the first exons of *aqp1a.1* and *aqp8a.1* (Fig. S4 and S5) were generated by
504 using cloning-independent protocol (Gagnon et al., 2014). Briefly, to generate templates for gRNA
505 transcription, a 60-base oligodeoxynucleotides containing the SP6 promoter sequence, the gene-
506 specific sequence (*aqp1a.1*: 5'-GACAGCTGGCCAGCAGACCC-3'; *aqp8a.1*: 5'-
507 GATGTCTCCCCCATCGCCCG-3') and 23-base overlap region was annealed to an 80-base
508 constant oligodeoxynucleotide encoding the reverse-complement of the tracrRNA tail. The ssDNA
509 overhangs were filled-in with T4 DNA polymerase (New England BioLabs) to generate dsDNA.
510 The gRNAs were *in vitro* transcribed using MEGAScript SP6 kit (Invitrogen), DNase treated and
511 purified with RNA Clean and Concentrator kit (Zymo Research). The gRNAs were quality-
512 checked by running 1 µg of the product on a 2% TBE-agarose gel. Cas9/gRNA RNP complex was
513 assembled just prior to injection and after 5 min incubation at room temperature 200 pg of Cas9
514 protein (Invitrogen) and 200 pg of gRNAs (100 pg of each, *aqp1a.1* gRNA and *aqp8a.1* gRNA)
515 were co-injected into one-cell stage *Tg(fli1:myr-mCherry)*^{ncv1} embryos. Such dose produced over
516 70% embryos survival post-injection showed CRISPR/Cas9-induced somatic *aqp1a.1* and
517 *aqp8a.1* gene mutations. F_0 founders were identified by outcrossing CRISPR/Cas9-injected fish
518 with wild type fish and screening the offspring for mutations at 2 dpf using Sanger sequencing.
519 We found one F_0 fish with germline transmitted mutations in both *aqp1a.1* and *aqp8a.1* genes and
520 outcrossed it with *Tg(fli1:myr-mCherry)*^{ncv1} and *Tg(fli1a:H2B-EGFP)*^{ncv69} transgenic fish to
521 establish F_1 generation of heterozygotes. A 55 F_1 fish were genotyped to identify 4 *aqp1a.1*$^{+/rk28}$,
522 *11 aqp8a.1*$^{+/rk29}$ and 12 *aqp1a.1*$^{+/rk28}$*;aqp8a.1*$^{+/rk29}$ heterozygote fish. Subsequently, F_1
523 heterozygote fish were in-crossed to establish a single and double homozygote fish.
524
525 **DNA isolation and genotyping.**
526 Genomic DNA was isolated from either embryos or fin clips using HotSHOT method (Meeker et
527 al., 2007). To identify genomic lesions, the following primers were used: aqp1a1-fwd (5'-

528 CGCCTCCAGATTCATTAGCAGGA-3') and aqp1a1-rev (5'-
529 GTAAGTGAACTGCTGCCAGTGA-3') to amplify a 550 bp fragment, and aqp8a1-fwd (5-
530 GGATCAATTGAGTTGCATAACAGAC-3') and aqp8a1-rev (5'-
531 CTGTAATGTAGACTTGTAAAGTGGA-3') to amplify a 638 bp fragment. Mutations were
532 assessed by direct sequencing of purified PCR products.
533
534 **Quantitative real-time PCR.**
535 Total RNA from whole embryos was isolated with TRI reagent using Direct-zol RNA MicroPrep
536 kit (Zymo Research) according to the manufacturer's protocol, including on-column DNA
537 digestion. RNA was quantified using a NanoDrop 1000 spectrophotometer (ThermoFisher
538 Scientific, USA). cDNA was synthesized from 300 ng of purified RNA using LunaScript RT
539 SuperMix kit (New England BioLabs) according to the manufacturer's protocol. Amplification of
540 target cDNA was performed in technical triplicate of three biological replicates using the SYBR
541 green methods. Each qPCR reaction mixture contained 5 µL 2x Luna Universal qPCR master mix
542 (New England BioLabs), 1 µL cDNA (2-fold dilution), 0.2 µL antarctic thermolabile UDG (New
543 England BioLabs) and 250 nM each primer to a final volume of 10 µL. Reactions were run in 384-
544 well plates (Applied Biosystems) using the QuantStudio 5 Real-Time PCR system (Applied
545 Biosystems) with the following thermal cycling conditions: initial UDG treatment at 25^0C for 2
546 minutes, UDG inactivation at 50^0C for 5 min and denaturation at 95^0C for 1 minutes, followed by
547 45 cycles of 15 sec at 95^0C, 30 sec at 60^0C with a plate read at the end of the extension step.
548 Control reactions included a no-template control (NTC) and a no-reverse transcriptase control
549 (NRT). Dissociation analysis of the PCR products was performed by running a gradient from 60
550 to 95^0C to confirm the presence of a single PCR product. Amplification data was analyzed using
551 QuantStudio Design and Analysis software v1.5.3 (Applied Biosystems) and relative fold change
552 was calculated using Pfaffl method (Pfaffl, 2001) and normalized to *gapdh* expression (as an
553 internal control). Primers are listed in Supplementary Table 2. Two embryos were used in each
554 biological replicate to generate an average value that was used to calculate the final mean ± SD
555 from two or three independent experiments.
556
557 **RNA *in situ* hybridization.**

558 **RNAscope *in situ* hybridization.** RNAscope® *in situ* hybridization was conducted by using
559 RNAscope Multiplex Fluorescent Reagent kit v2 (Advanced Cell Diagnostics). We adapted
560 manufacture's protocol designed for samples mounted on slides and protocol developed for whole-
561 mount embryo samples (Gross-Thebing et al., 2014). For each experimental point, 5 embryos were
562 processed in one 1.5 ml Eppendorf tube. Briefly, 20 and 22 hpf old embryos were manually
563 dechorionated and fixed in freshly prepared 4% methanol-free PFA in PBS for 1 hour at room
564 temperature. After fixation, embryos were washed three times in PBS containing 0.01% Tween-
565 20 (PBST), dehydrated stepwise in 5-min washes in a series of increasing methanol concentrations
566 (25%, 50%, 75%, 100%) in PBS and then stored in 100% methanol at -20^{0}C before use them for
567 hybridization. The methanol-stored embryos were incubated with 5% H_2O_2 in methanol for 20 min
568 at room temperature and then rehydrated stepwise in 5-min washes in series of decreasing
569 methanol concentrations (75%, 50%, 25%) in PBS, followed by three times 5-min washes in PBST.
570 Embryos were permeabilized in 2 drops of RNAscope® Protease III for 15 min, rinsed three times
571 with PBST and hybridized with RNAscope target probes overnight at 50^{0}C in water bath. After
572 hybridization probes were recovered and embryos were washed three times with 0.2x SSCT
573 [0.01% Tween-20 in SSC] at room temperature, re-fixed with 4% PFA for 10 min, and washed
574 three times with 0.2x SSCT. For RNA detection, the embryos were first hybridized with three
575 different amplifier solution for 30 min (Amp1, and Amp2) and 15 min (Amp3) in a water bath at
576 40^{0}C. After each hybridization step, the embryos were washed three times with 0.2x SSCT for 10
577 min at room temperature. To develop signal of each probe, the embryos were sequentially
578 incubated in a water bath at 40^{0}C with: (i) the horseradish peroxidase (HRP) for 15 min, (ii) TSA
579 fluorophore for 30 min and (iii) the HRP blocker for 15 min. After each incubation step, the
580 embryos were washed three times with 0.2x SSCT for 10 min at room temperature. HRP step is
581 linked to a probe channel, we first developed C1 probe, *Dr-aqp1a.1* (Advanced Cell Diagnostics)
582 using HRP-C1 and TSA Vivid Fluorophore 520 (Tocris, dilution 1:1500), then C2 probe, *Dr-*
583 *lrrc8aa* (Advance Cell Diagnostics) using HRP-C2 and TSA Vivid Fluorophore 570 (Tocris,
584 dilution 1:1500), and finally C3 probe, *Dr-aqp8a.1* (Advanced Cell Diagnostics) using HRP-C3
585 and TSA Vivid Fluorophore 650 (Tocris, dilution 1:1500). Nuclei were counterstained with DAPI
586 ready-to-use solution overnight at 4^{0}C in the dark. Prior to imaging embryos were rinsed in PBST
587 and kept in 70% glycerol in PBS at 4^{0}C in the dark. Images were acquired using Olympus FV3000
588 confocal microscope and an Olympus UPlanXApo 60x/NA 1.42 oil immersion objective.

589 **Chromogenic *in situ* hybridization.** Chromogenic *in situ* hybridization was conducted according
590 to standard protocol (Thisse and Thisse, 2007) with minor modifications. For each experimental
591 point, 10 embryos were processed in one 1.5 ml Eppendorf tube. Briefly, 30, 48, 72 and 96 hpf old
592 embryos were manually dechorionated and fixed in freshly prepared 4% methanol-free PFA in
593 PBS (pH 7.4) at 4^0C overnight. After fixation embryos were washed three times in PBS containing
594 0.1% Tween-20 (PBST), dehydrated stepwise in 5-min washes in a series of increasing methanol
595 concentrations (25%, 50%, 75%, 100%) in PBS and then stored in 100% methanol at -20^0C before
596 use them for hybridization. The methanol-stored embryos were rehydrated stepwise in 5-min
597 washes in series of decreasing methanol concentrations (75%, 50%, 25%) in PBS followed by
598 three times 5-min washes in PBST, and permeabilized 20 min with 10 µg/mL proteinase K
599 (ThermoFisher Scientific). Hybridization was carried out in buffer [50% formamide, 5x SSC, 50
600 g/mL heparin, 500 g/mL tRNA (Roche) and 0.1% Tween-20] containing 5% dextran sulfate
601 (MW=500 kDa) at 69^0C overnight. After stringency wash, the specimens were blocked with 2%
602 blocking reagent (Roche) in maleic acid buffer [100 mM maleic acid, 150 mM NaCl, 50 mM
603 $MgCl_2$ and 0.1% Tween-20, pH 7.5] and incubated overnight with anti-digoxigenin antibody,
604 conjugated with alkaline phosphatase (dilution 1:5000, Roche) at 4^0C. For detection of alkaline
605 phosphatase, specimens were incubated in staining buffer [50 mM Tris-HCl, 50 mM NaCl, 25 mM
606 $MgCl_2$, 2% Polyvinyl alcohol and 0.1% Tween-20, pH 9.5] containing 375 µg/mL nitro-blue
607 tetrazolium chloride (Roche) and 175 µg/mL 5-bromo-4-chloro-3'-indolyl-phosphate (Roche).
608 Embryos were cleared in 70% glycerol overnight and imaged using Leica M205FA microscope.
609 **RNA probe synthesis.** The cDNA-containing vectors were linearized with appropriate restriction
610 enzymes (detailed maps of vectors will be provided upon request) and used as a template for RNA
611 probe synthesis. Sense and antisense RNA probes were synthesized using MEGAscript SP6 or T7
612 kits (Invitrogen) and digoxigenin (DIG)-labeled rNTPs (Roche) according to the manufacturer's
613 protocol and purified using RNA Clean and Concentrator kit (Zymo Research). The following
614 sense and antisense DIG-labeled riboprobes were generated: (i) *aqp1a.1*, 1.1 kb long probe
615 comprised 121 nt of 5'UTR, 783 nt of the open reading frame (ORF) and 207 nt of 3'UTR; (ii)
616 *aqp8a.1*, 0.8 kb long probe comprised 17 nt of 5'UTR, 783 nt of ORF and 30 nt of 3'UTR. Sense
617 probes showed no specific or unspecific staining (data not shown).

618 **Image processing.** Chromogenic and RNAscope *in situ* hybridization images were processed
619 using ImageJ software (NIH, version 2.9.0/1.53t) with brightness and contrast adjustments. Z-
620 stacks of fluorescent images are presented as maximum intensity projections.
621
622 **Analysis of mRNA expression in tip and stalk cells.**
623 RNAscope processed embryos were mounted on slide and imaged using Olympus FV3000
624 confocal microscope and Olympus UPlanXApo 60x/NA 1.42 oil immersion objective. Maximum
625 intensity projection of z-stacks was used to determine the level of cellular fluorescence in ImageJ.
626 The tip and stalk cells were selected using freehand selection tool, "mean grey value", "area" and
627 "integrated density" in each ROI were measured first for channel 1 (aqp1a.1). A region next to cell
628 that has no fluorescence was selected as background and measured. The step was repeated for
629 channel 2 (aqp8a.1) on the same ROIs. Two parameters were calculated for each channel, (i) the
630 corrected total cell fluorescence, CTCF=Integrated Density – (Area of selected cell x Mean
631 fluorescence of background) and (ii) ratio, R=CTCF of tip cell/CTCF of stalk cell. We consider
632 that if R <0.9, expression is lower in tip cell, if R=0.9-1.1, expression is equal in tip and stalk cells,
633 if R>1.1, expression is higher in tip cell.
634
635 **Imaging.**
636 For live confocal imaging, embryos were mounted in 0.8% low-melt agarose (Bio-Rad) in E3
637 medium containing 0.16 mg/mL Tricaine (Sigma-Aldrich) and 0.003% phenylthiourea (Sigma-
638 Aldrich) in glass bottom 35-mm dishes (MatTek). Confocal Z-stacks were acquired using an
639 inverted Olympus IX83/Yokogawa CSU-W1 spinning disc confocal microscope equipped with a
640 Zyla 4.2 CMOS camera (Andor) and Olympus UPLSAPO 40x/NA 1.25 or 30x/NA 1.05 silicone
641 oil immersion objectives. Bright-field images were acquired on Leica M205FA microscope.
642 Images were processed using ImageJ software (NIH, version 2.9.0/1.53t).
643
644 **Analysis of cell migration.**
645 *aqp1a.1*$^{+/rk28}$*;aqp8a.1*$^{+/rk29}$ and *aqp1a.1*$^{rk28/rk28}$*;aqp8a.1*$^{rk29/rk29}$ embryos on *Tg(fli1a:H2B-*
646 *EGFP)*^{ncv69}*;(fli1:Lifeact-mCherry)*^{ncv7} double transgenic background were imaged from 21 to 30
647 hpf with time interval 6 min using Olympus UPLSAPO 30x/NA 1.05 silicon oil immersion
648 objective. We tried to mount both heterozygote and mutant embryos on the same dish (1 het plus

649 2 mut, or 2 het plus 2 mut) to image embryos on the same experimental conditions. Acquired time-
650 lapse images were registered using HyperStackReg plugin in ImageJ, tip cell and nuclei were
651 tracked using Manual Tracking plugin and velocity was calculated.
652
653 **Analysis of grow rate of actin bundles in filopodia.**
654 Wild type and *aqp1a.1*$^{rk28/rk28}$*;aqp8a.1*$^{rk29/rk29}$ embryos on *Tg(fli1ep:EGFP-*
655 *PLC1δPH)*^{rk26}*;(fli1:Lifeact-mCherry)*^{ncv7} double transgenic background were imaged starting from
656 25 hpf for 10 min with time interval 30 sec using Olympus UPLSAPO 60x/NA 1.2 water
657 immersion objective. Actin bundles growth was tracked using Manual Tracking plugin and
658 velocity was calculated.
659
660 **Analysis of filopodia number and length.**
661 Wild type, *aqp1a.1*$^{+/rk28}$*;aqp8a.1*$^{+/rk29}$ and *aqp1a.1*$^{rk28/rk28}$*;aqp8a.1*$^{rk29/rk29}$ embryos on
662 *Tg(fli1ep:EGFP-PLC1δPH)*^{rk26}*;(fli1:Lifeact-mCherry)*^{ncv7} double transgenic background were
663 imaged starting from 24 hpf for 30 min with time interval of 50 sec using Olympus UPLSAPO
664 60x/NA 1.2 water immersion objective. In a single image we counted filopodia number per vessel,
665 measured membrane length and calculated filopodia number.
666
667 **Assessment of tip cell polarization.**
668 *Tg(kdrl:nls-EGFP)*^{ubs1}*;(fli1:Has.B4GALT1-mCherry)*^{bns9Tg} wildtype and *aqp8a.1*$^{rk29/rk29}$ embryos
669 were imaged at 24-26 hpf using an Olympus UPLSAPO 40x/NA 1.25 silicon oil immersion
670 objective. To analyze endothelial tip cell polarity in *aqp1a.1*$^{rk28/rk29}$ embryos, Golgi apparatus and
671 nuclei were labelled by mosaic expression of *pDs-fli1ep:nls-EGFP-P2A-mKate2-GM130* plasmid.
672 Images were analyzed using Fiji (NIH). To assess polarity, the nucleus was fit into an ellipsoid
673 shape and the angle between the primary axis of the ellipse and the center of the Golgi was
674 measured (Fig. S10D). Polarization of ECs is defined as follows: (1) front (polarized), if the Golgi
675 is located within $-30^0 \sim +30^0$; (2) none, if the Golgi is located within $+30^0 \sim +150^0$ or $-30^0 \sim -150^0$;
676 or (3) rear, if the Golgi is located on the downstream side of the nucleus and angle is $-150^0 \sim +150^0$.
677 Tip cells in ISVs no. 5-15 were analyzed.
678
679 **Quantification of EC number and ISV diameter.**

680 Measurements were performed in wildtype, *aqp1a.1*$^{rk28/rk28}$, *aqp8a.1*$^{rk29/rk29}$ and
681 *aqp1a.1*$^{rk28/rk28}$*;aqp8a.1*$^{rk29/rk29}$ zebrafish raised in *Tg(fli1:Lifeact-mCherry)*^{ncv7}*;(fli1a:H2B-*
682 *EGFP)*^{ncv69} transgenic line or in *Tg(fli1ep:aqp1a.1-mEmerald)*^{rk30}*;(fli1:myr-mCherry)*^{ncv1} and
683 *Tg(fli1ep:aqp8a.1-mEmerald)*^{rk31}*; (fli1:myr-mCherry)*^{ncv1} zebrafish. Confocal z-stacks images of
684 embryos were taken at 50 - 54 hpf and 3 dpf using Olympus UPLSAPO 40x/NA 1.25 silicone oil
685 immersion objective. ISVs no. 5 to 15 were used for quantification. For ISV diameter, 5
686 measurements were made along the length of each ISV using ImageJ (NIH) and the average was
687 plotted.
688
689 **Chemical treatment.**
690 Latrunculin B (Merck Millipore) was dissolved in DMSO to 1 mg/ml and stored at -20^{0}C. Ki8751
691 (Selleck Chemicals) was prepared as 5 mM solution in DMSO and stored at -80^{0}C. DCPIB (Tocris)
692 was prepared as 10 mM solution in EtOH and stored at -20^{0}C. All compounds were diluted to the
693 desired concentration in E3 medium (see in figure legends). Embryos were treated from 20 hpf for
694 6 (Ki8751 and DCPIB) or 8 hours (Latrunculin B). For imaging experiments, the same
695 concentrations of chemicals were added to the agarose and E3 medium.
696
697 **Cell culture.**
698 Adult human aortic endothelial cells (HAEC) (Lonza, lot-20TL231227) were cultured in EGM
699 medium (Lonza) and used at passage 3. Cells were seeded in EBM medium (Lonzo) supplemented
700 with 2% FBS (Gibco) at 4 x 10^5 cells/well on 24-well plate (Trueline) coated with 5 μg/ml
701 fibronectin (Sigma-Aldrich). Cells were treated with either 0.01% DMSO or different
702 concentrations of Ki8751 inhibitor for 6 hours. Cells were lysed with TRI reagent and RNA was
703 isolated using Direct-zol RNA MicroPrep kit (Zymo Research).
704
705 **Single-cell RNA sequencing.**
706 ECs were isolated from *Tg(kdrl:EGFP)*^{s843} transgenic embryos. Cell sorting was carried out with
707 FACSAriaII Cell Sorter (BD Bioscience). Single-cell suspension was loaded into the 10X
708 Chromium system and cDNA libraries were constructed using Chromium Next GEM Single Cell
709 3′ GEM, Library and Gel Bead Kit v2 (10X Genomics) according to manufacturer's protocol.
710 Library was sequenced on the Illumina HiSeq 1500 Sequencer (Illumina, USA). Cell Ranger v2.1

711 was used to de-multiplex raw base call (BCL) files generated by Illumina sequencers into FASTQ
712 files.
713
714 **Single-cell RNA sequencing data analysis.**
715 The raw sequence data from above mentioned internal sequencing and also a public zebrafish
716 embryo data at 24 hpf stage (Gurung et al., 2022) were processed. The public dataset was obtained
717 from NCBI GEO database (accession number GSE202912). The raw sequencing reads from both
718 datasets were mapped to the zebrafish genome assembly (GRCz11, Ensembl release 112). Further
719 analyses were performed using Seurat package (version 4.3.0) in R software (https://www.r-
720 project.org). The expression matrices were first filtered by keeping genes that are expressed in a
721 minimum of 3 cells and cells that expressed a minimum of 200 genes for downstream analysis.
722 The data were then normalized using NormalizeData function which normalizes the gene
723 expression for each cell by the total expression counts (with a scale factor 10,000). To correct for
724 batch effect between the data from the two-time points, the rpca method in the Seurat package was
725 applied to integrate the data. The top 2000 variable genes identified using the vst method in
726 FindVariableFeatures function were used for principal component analysis in RunPCA function,
727 and the first 30 principal components were used for visualization analysis with Uniform Manifold
728 Approximation and Projection (UMAP) method, and in FindNeighbors function analysis. The cell
729 clustering resolution was set at 0.5 in FindClusters function. The Seurat object was then processed
730 using the ShinyCell package (version: 2.1.0) for gene expression visualizations.
731
732 **Statistical analysis.**
733 Statistical analysis was performed using Prism software version 10.2.0 (GraphPad). The variance
734 between the mean values of two groups was evaluated using the unpaired Student's *t*-test. For
735 assessment of more than three groups, we used one-way analysis of variance (ANOVA) test. A *P*
736 value of <0.05 was considered statistically significant. Statistic details can be found in each figure
737 legend.
738
739 **Data availability.**

740 The scRNA-seq raw data from this study is available at NCBI's Gene Expression Omnibus
741 database (accession number GSE262232). The data supporting the fundings of this study are
742 available from the corresponding author upon reasonable request.
743
744 **Acknowledgements**
745 We thank members of the Phng Lab, Y-C. Wang and S. Thukral for discussions and suggestions;
746 G. Chen, E. Taniguchi, RIKEN BDR Research Aquarium and RIKEN Kobe BioImaging Facilities
747 & Factory for technical assistance; J. Vermot, M. Francois and A. Yap for comments on the
748 manuscript. This work was supported by core funding from RIKEN BDR (to L.K.P.), RIKEN
749 BDR-Otsuka Pharmaceutical Collaboration Center (I.K.), the Naito Foundation (L.K.P.), the JSPS
750 Grants-in-Aid for Scientific Research (KAKENHI) grants (22H02624, 22H05168 to L.K.P;
751 22K06244 to I.K.), Swedish Research Council (2015-00550 to C.B.); Swedish Cancer Society
752 (2018/449, 2018/1154 to C.B.); Knut and Alice Wallenberg Foundation (2020.0057, 2018.0218 to
753 C.B.); Swedish Brain Foundation (ALZ2019-0130, ALZ2022-0005 to C.B.); the Leducq
754 Foundation (22CVD01, 23CVD02 to C.B.) and the Innovative Medicines Initiative (IM2PACT-
755 807015 to C.B.)
756
757 **Authorship contributions**
758 Conceptualization: L.K.P.; Methodology: I.K., L.H., H.W. and L.K.P.; Formal analysis: I.K. and
759 L.H.; Resources: C.B. and L.K.P.; Writing: I.K. and L.K.P; Supervision: L.K.P.
760
761 **Declaration of interests**
762 The authors declare no competing interests.
763
764 **Figure legends**
765
766 **Figure 1. Differential expression of *aqp1a.1* and *aqp8a.1* mRNAs in tip and stalk cells.**
767 (**A-F**) Detection of *aqp1a.1* and *aqp8a.1* mRNA by RNAscope *in situ* hybridization in 20 (A - D)
768 and 22 (E and F) hpf embryos. Representative maximum intensity projection of confocal z-stacks
769 of tip and stalk cells sprouting from DA are shown (n = 9 embryos, 2 independent experiments).

770 B and F show magnified region of a tip cell from a 20 and 22 hpf zebrafish, respectively (tip cell
771 and EC nuclei in the DA are outlined). Scale bar, 10 µm (B and F) and 40 µm (A, C - E).
772 (**G**) Percentage of vascular sprouts with differential expression of *aqp1a.1* and *aqp8a.1* mRNA in
773 tip and stalk cells in 22 hpf embryos (n=23 sprouts from 8 embryos, 2 independent experiments).
774 (**H**) qPCR analysis of *aqp1a.1* and *aqp8a.1* expression in zebrafish embryos treated with 0.01%
775 DMSO or 1 µM ki8751 at 20 hpf for 6 hours (n = 3 independent experiments).
776 (**I**) qPCR analysis of *AQP1* gene expression in HAECs treated with 0.01% DMSO, 1 or 10 nM
777 ki8751 for 6 hours (n = 2 independent experiments).
778 In panels H and J, gene expressions are shown relative to *gapdh* expression and data are presented
779 as mean ± SD; statistical significance was determined by Brown-Forsythe and Welch ANOVA
780 tests with Dunnett's multiple comparisons test; ns $p>0.05$, $^{**}p<0.01$, $^{***}p<0.001$, and $^{****}p<0.0001$.
781 DA, dorsal aorta; PCV, posterior cardinal vein.
782 See also Fig. S1-S3.
783
784 **Figure 2. Aquaporin proteins are enriched at the leading edge of migrating tip cells.**
785 (**A-B**) Representative maximum intensity projection confocal z-stacks of endothelial tip cells of
786 25 hpf *Tg(fli1ep:aqp1a.1-mEmerald)*^{rk30}*;(kdrl:ras-mCherry)*^{s916} (A) and *Tg(fli1ep:aqp8a.1-*
787 *mEmerald)*^{rk31}*;(kdrl:ras-mCherry)*^{s916} (B) embryos. White serrated line outlines tip-stalk cell
788 border. Scale bar, 20 µm.
789 (**C-D**) Still images from time-lapse movies of migrating tip cells from *Tg(fli1ep:aqp1a.1-*
790 *mEmerald)*^{rk30} (C) and *Tg(fli1ep:aqp8a.1-mEmerald)*^{rk31} (D) embryos. Movies were taken from 24
791 to 30 hpf. Arrowheads, Aquaporin protein localization at the leading edge of migrating tip cells.
792 Arrows, Aquaporin localization in filopodia. Time, h:min. Scale bar, 5 µm.
793 See also Movies S1 and S2.
794
795 **Figure 3. Loss of Aquaporin function leads to defective trunk vessel formation.**
796 (**A-D**) Representative maximum intensity projection confocal z-stacks of 28 hpf
797 *aqp1a.1*$^{+/rk28}$*;aqp8a.1*$^{+/rk29}$ (A), *aqp1a.1*$^{rk28/rk28}$ (B), *aqp8a.1*$^{rk29/rk29}$ (C) and
798 *aqp1a.1*$^{rk28/rk28}$*;aqp8a.1*$^{rk29/rk29}$ (D) embryos.

799 (**E**) Quantification of ISV length at different positions along the trunk of 28 hpf embryos
800 (*aqp1a.1*$^{+/rk28}$*;aqp8a.1*$^{+/rk29}$: n = 21 embryos; *aqp1a.1*$^{rk28/rk28}$: n = 20 embryos; *aqp8a.1*$^{rk29/rk29}$: n =
801 20 embryos; *aqp1a.1*$^{rk28/rk28}$*;aqp8a.1*$^{rk29/rk29}$: n = 19 embryos from 2 independent experiments).
802 (**F**) Illustration of aISV and vISV connections in the trunk of wild type embryo at 3 dpf.
803 (**G-J**) Representative maximum intensity projection confocal z-stacks of 3 dpf wild type (G),
804 *aqp8a.1*$^{rk29/rk29}$ (H), *aqp1a.1*$^{rk28/rk28}$ (I), and *aqp1a.1*$^{rk28/rk28}$*;aqp8a.1*$^{rk29/rk29}$ (J) embryos. Asterisk
805 marks incomplete ISVs, arrows point EC nuclei on the contralateral side.
806 (**K**) Pie chart showing proportion of different classes of truncated ISV phenotypes (I-VI) found in
807 *aqp1a.1*$^{rk28/rk28}$*;aqp8a.1*$^{rk29/rk29}$ mutant embryos at 3 dpf.
808 DA, dorsal aorta; DLAV, dorsal longitudinal anastomotic vessel; ISV, intersegmental vessel; aISV,
809 arterial ISV; vISV, venous ISV; NC, notochord; NT, neural tube; PCV, posterior cardinal vein.
810 Scale bar, 50 µm (G-J) and 200 µm (A-D).
811 See also Fig. S6-S8.
812
813 **Figure 4. Aquaporins promote endothelial tip cell protrusion and migration.**
814 (**A**) Timing of tip cell emergence from the DA in *aqp1a.1*$^{+/rk28}$*;aqp8a.1*$^{+/rk29}$ (n = 23 cells) and
815 *aqp1a.1*$^{rk28/rk28}$*;aqp8a.1*$^{rk29/rk29}$ (n = 27 cells).
816 (**B-C**) Still images from time-lapse imaging of migrating tip cells from *aqp1a.1*$^{+/rk28}$*;aqp8a.1*$^{+/rk29}$
817 (B) and *aqp1a.1*$^{rk28/rk28}$*;aqp8a.1*$^{rk29/rk29}$ (C) embryos from 20 to 30 hpf. White arrows, retracting
818 tip cell. *, secondary sprouting from PCV. Scale bar, 10 µm.
819 (**D-E**) Stills images from representative time-lapse movies of migrating tip cells in
820 *aqp1a.1*$^{+/rk28}$*;aqp8a.1*$^{+/rk29}$ (D, n = 2) and *aqp1a.1*$^{rk28/rk28}$*;aqp8a.1*$^{rk29/rk29}$ (E, n = 5) embryos.
821 Movies were taken from 25 to 30 hpf (n = 2 independent experiments). Bracket, formation of stable
822 protrusions. Scale bar, 20 µm.
823 (**F-G**) Representative maximum intensity projection confocal z-stacks of tip cells from wild type
824 (F) and *aqp1a.1*$^{rk28/rk28}$*;aqp8a.1*$^{rk29/rk29}$ (G) embryos at 26 hpf. Scale bar, 10 µm.
825 (**H**) Quantification of filopodia number in tip cells of wild type (n = 36 cells from 10 embryos, 2
826 independent experiments), *aqp1a.1*$^{+/rk28}$*;aqp8a.1*$^{+/rk29}$ (n = 19 cells from 6 embryos, 2 independent
827 experiments) and *aqp1a.1*$^{rk28/rk28}$*;aqp8a.1*$^{rk29/rk29}$ (n = 28 cells from 9 embryos, 2 independent
828 experiments) embryos.

829 (**I**) Quantification of filopodia length in tip cells of wild type (n = 24 cells from 7 embryos, 2
830 independent experiments), *aqp1a.1*$^{+/rk28}$*;aqp8a.1*$^{+/rk29}$ (n = 16 cells from 7 embryos, 2 independent
831 experiments) and *aqp1a.1*$^{rk28/rk28}$*;aqp8a.1*$^{rk29/rk29}$ (n = 11 cells from 6 embryos, 2 independent
832 experiments) embryos.
833 (**J**) Quantification of growth rate of actin bundles in tip cell filopodia in 25 hpf wild type (n = 12
834 cells from 7 embryos, 2 independent experiments) and *aqp1a.1*^{rk28}*;aqp8a.1*^{rk29} (n = 12 cells from
835 6 embryos, 2 independent experiments) embryos.
836 (**K**) Quantification of tip cell leading edge displacement of *aqp1a.1*$^{+/rk28}$*;aqp8a.1*$^{+/rk29}$ (n = 19 cells
837 from 5 embryos, 3 independent experiments) and *aqp1a.1*$^{rk28/rk28}$*;aqp8a.1*$^{rk29/rk29}$ (n = 47 cells from
838 13 embryos, 6 independent experiments) embryos at 25 - 30 hpf.
839 (**L**) Quantification of tip cell nuclei displacement of *aqp1a.1*$^{+/rk28}$*;aqp8a.1*$^{+/rk29}$ (n = 20 cells from
840 6 embryos, 4 independent experiments) and *aqp1a.1*$^{rk28/rk28}$*;aqp8a.1*$^{rk29/rk29}$ (n = 20 cells from 4
841 embryos, 2 independent experiments) embryos at 21 - 30 hpf.
842 (**M**) Quantification of tip cell migration velocity in *aqp1a.1*$^{+/rk28}$*;aqp8a.1*$^{+/rk29}$ (n = 19 cells from
843 5 embryos, 3 independent experiments) and *aqp1a.1*$^{rk28/rk28}$*;aqp8a.1*$^{rk29/rk29}$ (n = 47 cells from 13
844 embryos, 6 independent experiments) embryos at 25 - 30 hpf.
845 Statistical significance was determined by Brown-Forsythe and Welch ANOVA tests with
846 Dunnett's (H) or Sidak's (I) multiple comparisons test, and with unpaired *t*-test (J, M). ns, $p>0.05$,
847 **, $p < 0.01$, ***, $p < 0.001$, and ****, $p < 0.0001$.
848 See also Fig. S10, Movies S3-6.
849
850 **Figure 5. Aquaporin-mediated water influx increases tip cell volume.**
851 (**A-C**) Representative maximum intensity projection confocal z-stacks of tip cell and its 3D-
852 volume rendering of 25 hpf wildtype (A), *aqp1a.1*$^{rk28/rk28}$*;aqp8a.1*$^{rk29/rk29}$ (B) and wildtype
853 embryos overexpressing Aqp1a.1 (C) labelled with cytosolic mEmerald or EGFP. Scale bar, 10
854 µm.
855 (**D**) Quantification of tip cell volume in 25 hpf wild type (n = 24 cells) and
856 *aqp1a.1*$^{rk28/rk28}$*;aqp8a.1*$^{rk29/rk29}$ (n = 20 cells) and wildtype overexpressing Aqp1a.1 (n = 32 cells)
857 embryos from 3 independent experiments. Statistical significance was determined by Brown-
858 Forsythe and Welch ANOVA tests. *, $p < 0.05$, **, $p < 0.01$, and ****, $p < 0.0001$.
859

860 **Figure 6. The chloride channel SWELL1 promotes EC migration and sprouting angiogenesis.**
861 (**A-B**) UMAP plots showing co-expression of *lrrc8aa* and *aqp1a.1* (A), and *lrrc8aa* and *aqp8a.1*
862 (B) in endothelial cells from 24 hpf, 34 hpf and 3 dpf embryos.
863 (**C-E**) Detection of *aqp1a.1*, *aqp8a.1* and *lrrc8aa* mRNA by RNAscope *in situ* hybridization in 22
864 hpf zebrafish embryo. Representative maximum intensity projection rendering of confocal z-
865 stacks of tip and stalk cells (C). D and E show surface rendering of image C where only endothelial
866 expression of *lrrc8aa* is shown after masking. Scale bar, 10 µm.
867 (**F-G**) Representative maximum intensity projection confocal z-stacks of 26 hpf wildtype embryos
868 treated with 0.05% EtOH (F) or 5 µM DCPIB (G) from 20 to 26 hpf (control, n = 16 embryos;
869 DCPIB, n = 18 embryos; 2 independent experiments). Scale bar, 50 µm.
870 (**H**) Quantification of ISV length in 26 hpf wildtype embryos treated with 0.05% EtOH or 5 µM
871 DCPIB (control, n = 133 vessels from 16 embryos; DCPIB, 157 vessels from 18 embryos; 2
872 independent experiments). Statistical significance was determined with unpaired *t*-test; ****, $p <$
873 0.0001.
874 (**I**) Quantification of tip cell leading edge displacement of wildtype embryos treated with 0.05%
875 EtOH (n = 29 cells from 7 embryos, 2 independent experiments) or 5 µM DCPIB (n = 29 cells
876 from 8 embryos, 3 independent experiments) at 25 - 30 hpf.
877 (**J**) Quantification of tip cell migration velocity in wildtype treated with 0.05% EtOH (n = 29 cells
878 from 7 embryos, 2 independent experiments) or 5 µM DCPIB (n = 29 cells from 8 embryos, 3
879 independent experiments) at 25 - 30 hpf. Statistical significance was determined with unpaired *t*-
880 test; ****, $p < 0.0001$.
881 (**K**) Quantification of filopodia number in tip cells of wildtype embryos treated with 0.05% EtOH
882 (n = 34 vessels from 9 embryos, 3 independent experiments) or 5 µM DCPIB (n = 53 vessels from
883 16 embryos, 3 independent experiments). Statistical significance was determined with unpaired *t*-
884 test; ****, $p < 0.0001$.
885 (**M-N**) Still images from representative time-lapse movies of migrating tip cells in wildtype
886 embryos treated with 0.05% EtOH (M, n = 7) or 5 µM DCPIB (N, n = 8). Movies were taken from
887 25 to 30 hpf (n = 3 independent experiments). Bracket, formation of stable protrusions. Scale bar,
888 20 µm.
889

890 **Figure 7. Additive function of actin polymerization and hydrostatic pressure in driving EC**
891 **migration and sprouting angiogenesis.**
892 (**A-D**) Representative maximum intensity projection confocal z-stacks of 28 hpf wild type (A and
893 B) and *aqp1a.1*$^{rk28/rk28}$*;aqp8a.1*$^{rk29/rk29}$ (C and D) embryos treated with 0.1% DMSO (A and C) or
894 0.8 µg/ml Lat. B (B and D) from 20 to 28 hpf (for each condition: wild type, n = 10 embryos;
895 *aqp1a.1*$^{rk28/rk28}$*;aqp8a.1*$^{rk29/rk29}$, n =12 embryos, 2 independent experiments). Scale bar, 20 µm.
896 (**E**) Quantification of ISV length in 28 hpf wild type and *aqp1a.1*$^{rk28/rk28}$*;aqp8a.1*$^{rk29/rk29}$ embryos
897 treated with 0.1% DMSO or 0.8 µg/ml Lat. B (wild type: n = 60 vessels from 10 control embryos,
898 n = 66 vessels from 10 Lat. B-treated embryos; *aqp1a.1*^{rk28}*;aqp8a.1*^{rk29}: n = 126 vessels from 12
899 control embryos, n = 112 vessels from 11 Lat. B-treated embryos, 2 independent experiments).
900 Statistical significance was determined by Brown-Forsythe ANOVA test with Sidak's multiple
901 comparison test; ns, *p,*>,0.05, **,$p < 0.01$, and ****, $p < 0.0001$. (**F**) Model of endothelial tip cell
902 migration. Tip cells generate membrane protrusions by actin polymerization and increased
903 hydrostatic pressure via Aquaporin-mediated water inflow. In the absence of actin polymerization
904 and presence of Aquaporins, hydrostatic pressure deforms membranes to generate membrane
905 protrusions. When Aquaporin function is lost, membrane protrusions is generated by actin
906 polymerization. Fewer membrane protrusions are formed when only one mechanism is utilized,
907 resulting in slower EC migration.
908 See also Movie S8.
909
910 **References**

911 Agre P, King LS, Yasui M, Guggino WB, Ottersen OP, Fujiyoshi Y, Engel A, Nielsen S. 2002.
912 Aquaporin water channels – from atomic structure to clinical medicine. *Journal of Physiology*
913 **542**:3–16. doi:10.1113/jphysiol.2002.020818

914 Ando K, Wang W, Peng D, Chiba A, Lagendijk AK, Barske L, Crump JG, Stainier DYR,
915 Lendahl U, Koltowska K, Hogan BM, Fukuhara S, Mochizuki N, Betsholtz C. 2019. Peri-
916 arterial specification of vascular mural cells from naïve mesenchyme requires Notch
917 signaling. *Development* **146**:dev165589-13. doi:10.1242/dev.165589

918 Bill BR, Korzh V. 2014. Choroid plexus in developmental and evolutionary perspective.
919 *Frontiers in Neuroscience* **8**:363. doi:10.3389/fnins.2014.00363

920 Boer LL de, Vanes L, Melgrati S, O'May JB, Hayward D, Driscoll PC, Day J, Griffiths A,
921 Magueta R, Morrell A, MacRae JI, Köchl R, Tybulewicz VLJ. 2023. T cell migration requires

922 ion and water influx to regulate actin polymerization. *Nature Communications* **14**:7844.
923 doi:10.1038/s41467-023-43423-8

924 Calamita G, Ferri D, Gena P, Liquori GE, Cavalier A, Thomas D, Svelto M. 2005. The Inner
925 Mitochondrial Membrane Has Aquaporin-8 Water Channels and Is Highly Permeable to
926 Water*. *Journal of Biological Chemistry* **280**:17149–17153. doi:10.1074/jbc.c400595200

927 Chae YK, Woo J, Kim M-J, Kang SK, Kim MS, Lee J, Lee SK, Gong G, Kim YH, Soria JC,
928 Jang SJ, Sidransky D, Moon C. 2008. Expression of Aquaporin 5 (AQP5) Promotes Tumor
929 Invasion in Human Non Small Cell Lung Cancer. *PLoS ONE* **3**:e2162.
930 doi:10.1371/journal.pone.0002162

931 Chan CJ, Costanzo M, Ruiz-Herrero T, Mönke G, Petrie RJ, Bergert M, Diz-Muñoz A,
932 Mahadevan L, Hiiragi T. 2019. Hydraulic control of mammalian embryo size and cell fate.
933 *Nature* **571**:112–116. doi:10.1038/s41586-019-1309-x

934 Chen C, Qin Y, Xu Y, Wang X, Lei W, Shen X, Chen L, Wang L, Gong J, Wang Y, Hu S, Liu
935 D. 2024. Aquaporins enriched in endothelial vacuole membrane regulate the diameters of
936 microvasculature in hyperglycaemia. *Cardiovascular Research* **120**:1065-1080.
937 doi:10.1093/cvr/cvae085

938 Choudhury MI, Benson MA, Sun SX. 2022. Trans-epithelial fluid flow and mechanics of
939 epithelial morphogenesis. *Seminars in Cell & Developmental Biology* **131**:146–159.
940 doi:10.1016/j.semcdb.2022.05.020

941 Chugh M, Munjal A, Megason SG. 2022. Hydrostatic pressure as a driver of cell and tissue
942 morphogenesis. *Seminars in Cell & Developmental Biology* **131**:134–145.
943 doi:10.1016/j.semcdb.2022.04.021

944 Clarke DN, Martin AC. 2021. Actin-based force generation and cell adhesion in tissue
945 morphogenesis. *Current Biology* **31**:R667–R680. doi:10.1016/j.cub.2021.03.031

946 Conner MT, Conner AC, Bland CE, Taylor LHJ, Brown JEP, Parri HR, Bill RM. 2012. Rapid
947 Aquaporin Translocation Regulates Cellular Water Flow. *Journal of Biological Chemistry*
948 **287**:11516–11525. doi:10.1074/jbc.m111.329219

949 Day RE, Kitchen P, Owen DS, Bland C, Marshall L, Conner AC, Bill RM, Conner MT. 2014.
950 Human aquaporins: regulators of transcellular water flow. *Biochimica et Biophysica Acta*
951 **1840**:1492–1506. doi:10.1016/j.bbagen.2013.09.033

952 Dumortier JG, Verge-Serandour ML, Tortorelli AF, Mielke A, Plater L de, Turlier H, Maître J-L.
953 2019. Hydraulic fracturing and active coarsening position the lumen of the mouse blastocyst.
954 *Science* **365**:465–468. doi:10.1126/science.aaw7709

955 Emelyanov A, Gao Y, Naqvi NI, Parinov S. 2006. Trans-Kingdom Transposition of the Maize
956 Dissociation Element. *Genetics* **174**:1095–1104. doi:10.1534/genetics.106.061184

957 Farinas J, Kneen M, Moore M, Verkman AS. 1997. Plasma Membrane Water Permeability of
958 Cultured Cells and Epithelia Measured by Light Microscopy with Spatial Filtering. *Journal of*
959 *General Physiology* **110**:283–296. doi:10.1085/jgp.110.3.283

960 Figueiredo AM, Barbacena P, Russo A, Vaccaro S, Ramalho D, Pena A, Lima AP, Ferreira RR,
961 Fidalgo MA, El-Marjou F, Carvalho Y, Vasconcelos FF, Lennon-Duménil A-M, Vignjevic
962 DM, Franco CA. 2021. Endothelial cell invasion is controlled by dactylopodia. *Proceedings*
963 *of the National Academy of Sciences* **118**:e2023829118. doi:10.1073/pnas.2023829118

964 Fukuhara S, Zhang J, Yuge S, Ando K, Wakayama Y, Sakaue-Sawano A, Miyawaki A,
965 Mochizuki N. 2014. Visualizing the cell-cycle progression of endothelial cells in zebrafish.
966 *Developmental Biology* **393**:10–23. doi:10.1016/j.ydbio.2014.06.015

967 Gagnon JA, Valen E, Thyme SB, Huang P, Akhmetova L, Ahkmetova L, Pauli A, Montague
968 TG, Zimmerman S, Richter C, Schier AF. 2014. Efficient mutagenesis by Cas9 protein-
969 mediated oligonucleotide insertion and large-scale assessment of single-guide RNAs. *PLoS*
970 *ONE* **9**:e98186. doi:10.1371/journal.pone.0098186

971 Gebala V, Collins R, Geudens I, Phng L-K, Gerhardt H. 2016. Blood flow drives lumen
972 formation by inverse membrane blebbing during angiogenesis in vivo. *Nature Cell Biology*
973 **18**:443–450. doi:10.1038/ncb3320

974 Gerhardt H, Golding M, Fruttiger M, Ruhrberg C, Lundkvist A, Abramsson A, Jeltsch M,
975 Mitchell C, Alitalo K, Shima D, Betsholtz C. 2003. VEGF guides angiogenic sprouting
976 utilizing endothelial tip cell filopodia. *Journal of Cell Biology* **161**:1163–1177.
977 doi:10.1083/jcb.200302047

978 Gradilone SA, Carreras FI, Lehmann GL, Marinelli RA. 2005. Phosphoinositide 3-kinase is
979 involved in the glucagon-induced translocation of aquaporin-8 to hepatocyte plasma
980 membrane. *Biology of the Cell* **97**:831–836. doi:10.1042/bc20040115

981 Gradilone SA, García F, Huebert RC, Tietz PS, Larocca MC, Kierbel A, Carreras FI, Larusso
982 NF, Marinelli RA. 2003. Glucagon induces the plasma membrane insertion of functional
983 aquaporin-8 water channels in isolated rat hepatocytes. *Hepatology* **37**:1435–1441.
984 doi:10.1053/jhep.2003.50241

985 Gross-Thebing T, Paksa A, Raz E. 2014. Simultaneous high-resolution detection of multiple
986 transcripts combined with localization of proteins in whole-mount embryos. *BMC Biology*
987 **12**:55. doi:10.1186/s12915-014-0055-7

988 Gunasekar SK, Xie L, Kumar A, Hong J, Chheda PR, Kang C, Kern DM, My-Ta C, Maurer J,
989 Heebink J, Gerber EE, Grzesik WJ, Elliot-Hudson M, Zhang Y, Key P, Kulkarni CA, Beals
990 JW, Smith GI, Samuel I, Smith JK, Nau P, Imai Y, Sheldon RD, Taylor EB, Lerner DJ,
991 Norris AW, Klein S, Brohawn SG, Kerns R, Sah R. 2022. Small molecule SWELL1 complex
992 induction improves glycemic control and nonalcoholic fatty liver disease in murine Type 2
993 diabetes. *Nature Communications* **13**:784. doi:10.1038/s41467-022-28435-0

994 Gurung S, Restrepo NK, Chestnut B, Klimkaite L, Sumanas S. 2022. Single-cell transcriptomic
995 analysis of vascular endothelial cells in zebrafish embryos. *Scientific Reports* **12**:13065.
996 doi:10.1038/s41598-022-17127-w

997 Herrera M, Garvin JL. 2007. Novel role of AQP-1 in NO-dependent vasorelaxation. *American*
998 *Journal of Physiology-Renal Physiology* **292**:F1443–F1451. doi:10.1152/ajprenal.00353.2006

999 Herrera M, Hong NJ, Garvin JL. 2006. Aquaporin-1 Transports NO Across Cell Membranes.
1000 *Hypertension* **48**:157–164. doi:10.1161/01.hyp.0000223652.29338.77

1001 Herwig L, Blum Y, Krudewig A, Ellertsdottir E, Lenard A, Belting H-G, Affolter M. 2011.
1002 Distinct cellular mechanisms of blood vessel fusion in the zebrafish embryo. *Current*
1003 *Biology* **21**:1942-1948. doi:10.1016/j.cub.2011.10.016

1004 Hogan BM, Bos FL, Bussmann J, Witte M, Chi NC, Duckers HJ, Schulte-Merker S. 2009. ccbe1
1005 is required for embryonic lymphangiogenesis and venous sprouting. *Nature Genetics* **41**:396-
1006 398. doi:10.1038/ng.321

1007 Jahn TP, Møller ALB, Zeuthen T, Holm LM, Klærke DA, Mohsin B, Kühlbrandt W, Schjoerring
1008 JK. 2004. Aquaporin homologues in plants and mammals transport ammonia. *FEBS Letters*
1009 **574**:31–36. doi:10.1016/j.febslet.2004.08.004

1010 Jin S-W, Beis D, Mitchell T, Chen J-N, Stainier DY. 2005. Cellular and molecular analyses of
1011 vascular tube and lumen formation in zebrafish. *Development* **132**: 5199-5209.
1012 doi:10.1242/dev.02087

1013 Jung HJ, Park J-Y, Jeon H-S, Kwon T-H. 2011. Aquaporin-5: A Marker Protein for Proliferation
1014 and Migration of Human Breast Cancer Cells. *PLoS ONE* **6**:e28492.
1015 doi:10.1371/journal.pone.0028492

1016 Karlsson T, Bolshakova A, Magalhães MAO, Loitto VM, Magnusson K-E. 2013. Fluxes of
1017 Water through Aquaporin 9 Weaken Membrane-Cytoskeleton Anchorage and Promote
1018 Formation of Membrane Protrusions. *PLoS ONE* **8**:e59901.
1019 doi:10.1371/journal.pone.0059901

1020 Kimmel CB, Ballard WW, Kimmel SR, Ullmann B, Schilling TF. 1995. Stages of embryonic
1021 development of the zebrafish. *Developmental dynamics* **203**:253--310.
1022 doi:10.1002/aja.1002030302

1023 Kondrychyn I, Garcia-Lecea M, Emelyanov A, Parinov S, Korzh V. 2009. Genome-wide
1024 analysis of Tol2 transposon reintegration in zebrafish. *BMC Genomics* **10**:418–418.
1025 doi:10.1186/1471-2164-10-418

1026 Kondrychyn I, Kelly DJ, Carretero NT, Nomori A, Kato K, Chong J, Nakajima H, Okuda S,
1027 Mochizuki N, Phng L-K. 2020. Marcksl1 modulates endothelial cell mechanoresponse to

1028 haemodynamic forces to control blood vessel shape and size. *Nature Communications*
1029 **11**:5476–18. doi:10.1038/s41467-020-19308-5

1030 Koun S, Kim J-D, Rhee M, Kim M-J, Huh T-L. 2016. Spatiotemporal expression pattern of the
1031 zebrafish aquaporin 8 family during early developmental stages. *Gene Expression Patterns*
1032 **21**:1–6. doi:10.1016/j.gep.2016.06.001

1033 Kozono D, Yasui M, King LS, Agre P. 2002. Aquaporin water channels: atomic structure
1034 molecular dynamics meet clinical medicine. *Journal of Clinical Investigation* **109**:1395–1399.
1035 doi:10.1172/jci15851

1036 Kwon H-B, Wang S, Helker CSM, Rasouli SJ, Maischein H-M, Offermanns S, Herzog W,
1037 Stainier DYR. 2016. In vivo modulation of endothelial polarization by Apelin receptor
1038 signalling. *Nature Communications* **7**:11805–12. doi:10.1038/ncomms11805

1039 Li Y, Konstantopoulos K, Zhao R, Mori Y, Sun SX. 2020. The importance of water and
1040 hydraulic pressure in cell dynamics. *Journal of Cell Science* **133**:jcs240341.
1041 doi:10.1242/jcs.240341

1042 Liu K, Nagase H, Huang CG, Calamita G, Agre P. 2006. Purification and functional
1043 characterization of aquaporin-8. *Biology of the Cell* **98**:153–161. doi:10.1042/bc20050026

1044 Loitto VM, Huang C, Sigal YJ, Jacobson K. 2007. Filopodia are induced by aquaporin-9
1045 expression. *Experimental Cell Research* **313**:1295–1306. doi:10.1016/j.yexcr.2007.01.023

1046 Loitto VM, Karlsson T, Magnusson K. 2009. Water flux in cell motility: Expanding the
1047 mechanisms of membrane protrusion. *Cell Motility and the Cytoskeleton* **66**:237–247.
1048 doi:10.1002/cm.20357

1049 Ma T, Yang B, Verkman AS. 1997. Cloning of a Novel Water and Urea-Permeable Aquaporin
1050 from Mouse Expressed Strongly in Colon, Placenta, Liver, and Heart. *Biochemical and*
1051 *Biophysical Research Communications* **240**:324–328. doi:10.1006/bbrc.1997.7664

1052 Maltaneri RE, Schiappacasse A, Chamorro ME, Nesse AB, Vittori DC. 2020. Aquaporin-1 plays
1053 a key role in erythropoietin-induced endothelial cell migration. *Biochimica et Biophysica Acta*
1054 *(BBA) - Molecular Cell Research* **1867**:118569. doi:10.1016/j.bbamcr.2019.118569

1055 Markou A, Unger L, Abir-Awan M, Saadallah A, Halsey A, Balklava Z, Conner M, Törnroth-
1056 Horsefield S, Greenhill SD, Conner A, Bill RM, Salman MM, Kitchen P. 2022. Molecular
1057 mechanisms governing aquaporin relocalisation. *Biochimica et Biophysica Acta (BBA) -*
1058 *Biomembranes* **1864**:183853. doi:10.1016/j.bbamem.2021.183853

1059 McLennan R, McKinney MC, Teddy JM, Morrison JA, Kasemeier-Kulesa JC, Ridenour DA,
1060 Manthe CA, Giniunaite R, Robinson M, Baker RE, Maini PK, Kulesa PM. 2019. Neural crest
1061 cells bulldoze through the microenvironment using Aquaporin 1 to stabilize filopodia.
1062 *Development* **147**:dev185231. doi:10.1242/dev.185231

1063 Meeker ND, Hutchinson SA, Ho L, Trede NS. 2007. Method for isolation of PCR-ready
1064 genomic DNA from zebrafish tissues. *Biotechniques* **43**:610–614. doi:10.2144/000112619

1065 Mosaliganti KR, Swinburne IA, Chan CU, Obholzer ND, Green AA, Tanksale S, Mahadevan L,
1066 Megason SG. 2019. Size control of the inner ear via hydraulic feedback. *eLife* **8**:e39596.
1067 doi:10.7554/elife.39596

1068 Munjal A, Lecuit T. 2014. Actomyosin networks and tissue morphogenesis. *Development*
1069 **141**:1789-1793. doi: 10.1242/dev.091645

1070 Murrell M, Oakes PW, Lenz M, Gardel ML. 2015. Forcing cells into shape: the mechanics of
1071 actomyosin contractility. *Nature Cell Biology* **16**:486–498. doi:10.1038/nrm4012

1072 Nagy TL, Strickland J, Weiner OD. 2023. Neutrophils actively swell to potentiate rapid
1073 migration. *bioRxiv* 2023.05.15.540704. doi:10.1101/2023.05.15.540704

1074 Nakajima H, Yamamoto K, Agarwala S, Terai K, Fukui H, Fukuhara S, Ando K, Miyazaki T,
1075 Yokota Y, Schmelzer E, Belting H-G, Affolter M, Lecaudey V, Mochizuki N. 2017. Flow-
1076 Dependent Endothelial YAP Regulation Contributes to Vessel Maintenance. *Developmental*
1077 *Cell* **40**:523-536.e6. doi:10.1016/j.devcel.2017.02.019

1078 Nakhoul NL, Davis BA, Romero MF, Boron WF. 1998. Effect of expressing the water channel
1079 aquaporin-1 on the CO2 permeability of Xenopus oocytes. *American Journal of Physiology-*
1080 *Cell Physiology* **274**:C543–C548. doi:10.1152/ajpcell.1998.274.2.c543

1081 Parab S, Quick RE, Matsuoka RL. 2021. Endothelial cell-type-specific molecular requirements
1082 for angiogenesis drive fenestrated vessel development in the brain. *eLife* **10**:e64295.
1083 doi:10.7554/elife.64295

1084 Pfaffl MW. 2001. A new mathematical model for relative quantification in real-time RT–PCR.
1085 *Nucleic Acids Research* **29**:e45–e45. doi:10.1093/nar/29.9.e45

1086 Phng L-K, Stanchi F, Gerhardt H. 2013. Filopodia are dispensable for endothelial tip cell
1087 guidance. *Development* **140**:4031–4040. doi:10.1242/dev.097352

1088 Prasad GV, Coury LA, Finn F, Zeidel ML. 1998. Reconstituted aquaporin 1 water channels
1089 transport CO2 across membranes. *Journal of Biological Chemistry* **273**:33123–33126.
1090 doi:10.1074/jbc.273.50.33123

1091 Preston GM, Carroll TP, Guggino WB, Agre P. 1992. Appearance of water channels in Xenopus
1092 oocytes expressing red cell CHIP28 protein. *Science* **256**:385–387.
1093 doi:10.1126/science.256.5055.385

1094 Qiu Z, Dubin AE, Mathur J, Tu B, Reddy K, Miraglia LJ, Reinhardt J, Orth AP, Patapoutian A.
1095 2014. SWELL1, a Plasma Membrane Protein, Is an Essential Component of Volume-
1096 Regulated Anion Channel. *Cell* **157**:447–458. doi:10.1016/j.cell.2014.03.024

1097 Rehn K, Wong KS, Balciunas D, Sumanas S. 2011. Zebrafish enhancer trap line recapitulates
1098 embryonic aquaporin 1a expression pattern in vascular endothelial cells. *International*
1099 *Journal of Developmental Biology* **55**:613–618. doi:10.1387/ijdb.103249kp

1100 Saadoun S, Papadopoulos MC, Hara-Chikuma M, Verkman AS. 2005. Impairment of
1101 angiogenesis and cell migration by targeted aquaporin-1 gene disruption. *Nature* **434**:786–
1102 792. doi:10.1038/nature03460

1103 Sauteur L, Affolter M, Belting H-G. 2017. Distinct and redundant functions of Esama and VE-
1104 cadherin during vascular morphogenesis. *Development* **144**:1554–1565.
1105 doi:10.1242/dev.140038

1106 Siekmann AF, Affolter M, Belting H-G. 2013. The tip cell concept 10 years after: New players
1107 tune in for a common theme. *Experimental Cell Research* **319**:1255–1263.
1108 doi:10.1016/j.yexcr.2013.01.019

1109 Soria LR, Fanelli E, Altamura N, Svelto M, Marinelli RA, Calamita G. 2010. Aquaporin-8-
1110 facilitated mitochondrial ammonia transport. *Biochemical and Biophysical Research*
1111 *Communications* **393**:217–221. doi:10.1016/j.bbrc.2010.01.104

1112 Stroka KM, Jiang H, Chen S-H, Tong Z, Wirtz D, Sun SX, Konstantopoulos K. 2014. Water
1113 permeation drives tumor cell migration in confined microenvironments. *Cell* **157**:611–623.
1114 doi:10.1016/j.cell.2014.02.052

1115 Talbot K, Kwong RWM, Gilmour KM, Perry SF. 2015. The water channel aquaporin-1a1
1116 facilitates movement of CO2 and ammonia in zebrafish (Danio rerio) larvae. *Journal of*
1117 *Experimental Biology* **218**:3931–3940. doi:10.1242/jeb.129759

1118 Thisse C, Thisse B. 2007. High-resolution in situ hybridization to whole-mount zebrafish
1119 embryos. *Nature Protocols* **3**:59–69. doi:10.1038/nprot.2007.514

1120 Tingaud-Sequeira A, Calusinska M, Finn RN, Chauvigné F, Lozano J, Cerdà J. 2010. The
1121 zebrafish genome encodes the largest vertebrate repertoire of functional aquaporins with dual
1122 paralogy and substrate specificities similar to mammals. *BMC Evolutionary Biology* **10**:38.
1123 doi:10.1186/1471-2148-10-38

1124 Voss FK, Ullrich F, Münch J, Lazarow K, Lutter D, Mah N, Andrade-Navarro MA, Kries JP
1125 von, Stauber T, Jentsch TJ. 2014. Identification of LRRC8 Heteromers as an Essential
1126 Component of the Volume-Regulated Anion Channel VRAC. *Science* **344**:634–638.
1127 doi:10.1126/science.1252826

1128 Wakayama Y, Fukuhara S, Ando K, Matsuda M, Mochizuki N. 2015. Cdc42 Mediates Bmp-
1129 Induced Sprouting Angiogenesis through Fmnl3-Driven Assembly of Endothelial Filopodia in
1130 Zebrafish. *Developmental Cell* **32**:109–122. doi:10.1016/j.devcel.2014.11.024

1131 Wang Y, Cohen J, Boron WF, Schulten K, Tajkhorshid E. 2007. Exploring gas permeability of
1132 cellular membranes and membrane channels with molecular dynamics. *Journal of Structural*
1133 *Biology* **157**:534–544. doi:10.1016/j.jsb.2006.11.008

1134 Wu DQ, Yang ZF, Wang KJ, Feng XY, Lv ZJ, Li Y, Jian ZX. 2017. AQP8 inhibits colorectal
1135 cancer growth and metastasis by down-regulating PI3K/AKT signaling and PCDH7
1136 expression. *American Journal of Cancer Research* **8**:266–279.

1137 Zeidel ML, Ambudkar SV, Smith BL, Agre P. 1992. Reconstitution of functional water channels
1138 in liposomes containing purified red cell CHIP28 protein. *Biochemistry* **31**:7436–7440.
1139 doi:10.1021/bi00148a002

1140 Zhang Y, Li Y, Thompson KN, Stoletov K, Yuan Q, Bera K, Lee SJ, Zhao R, Kiepas A, Wang
1141 Y, Mistriotis P, Serra SA, Lewis JD, Valverde MA, Martin SS, Sun SX, Konstantopoulos K.
1142 2022. Polarized NHE1 and SWELL1 regulate migration direction, efficiency and metastasis.
1143 *Nature Communications* **13**:6128. doi:10.1038/s41467-022-33683-1

Figure 1

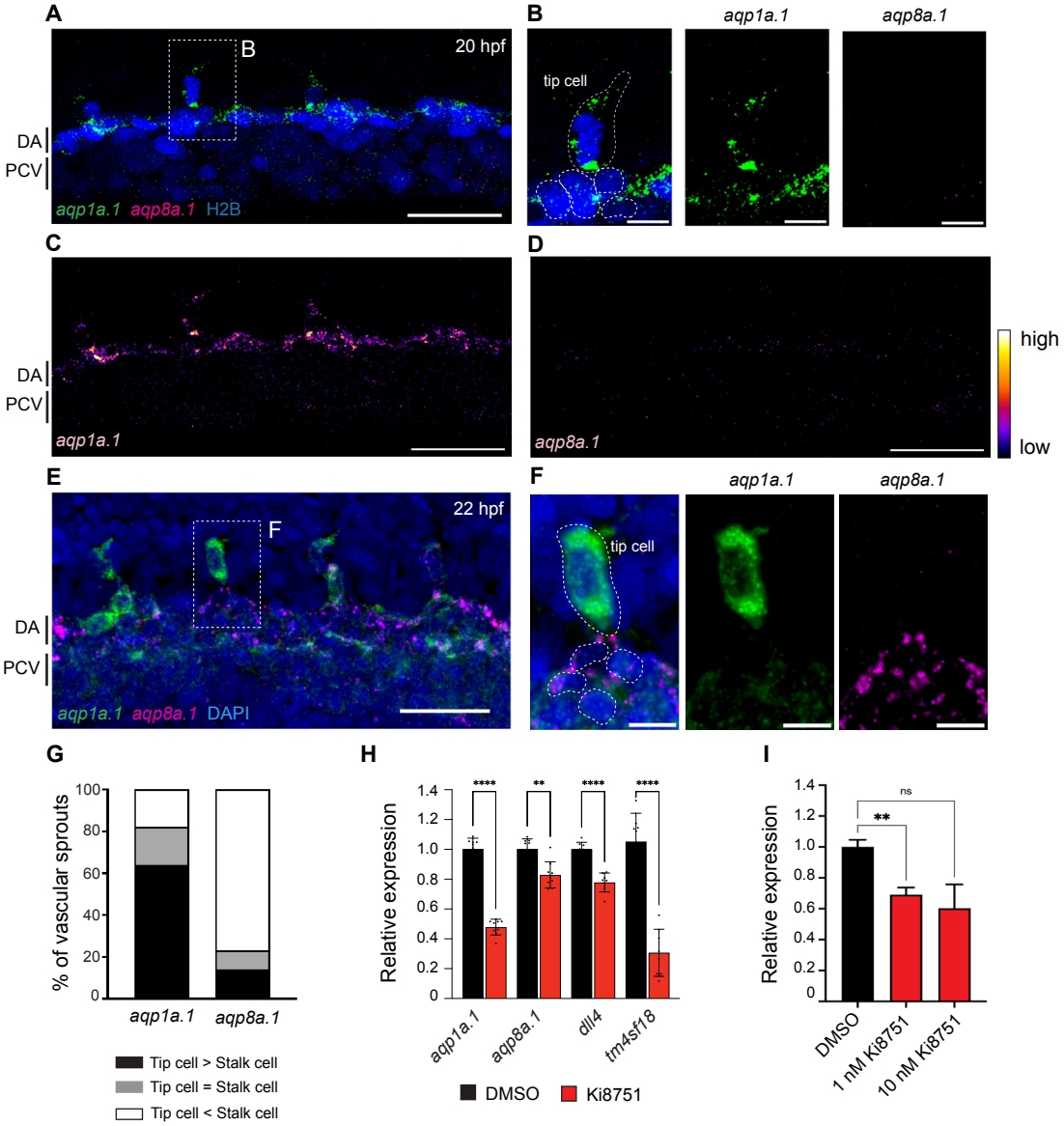
A
B
20 hpf
DA
PCV
aqp1a.1 aqp8a.1 H2B
B
aqp1a.1
aqp8a.1
tip cell
C
D
DA
PCV
aqp1a.1
aqp8a.1
high
low
E
F
22 hpf
DA
PCV
aqp1a.1 aqp8a.1 DAPI
F
aqp1a.1
aqp8a.1
tip cell
G
% of vascular sprouts
aqp1a.1
aqp8a.1
Tip cell > Stalk cell
Tip cell = Stalk cell
Tip cell < Stalk cell
H
Relative expression
aqp1a.1
aqp8a.1
dll4
tm4sf18
DMSO
Ki8751
I
Relative expression
ns
DMSO
1 nM Ki8751
10 nM Ki8751

Figure 2

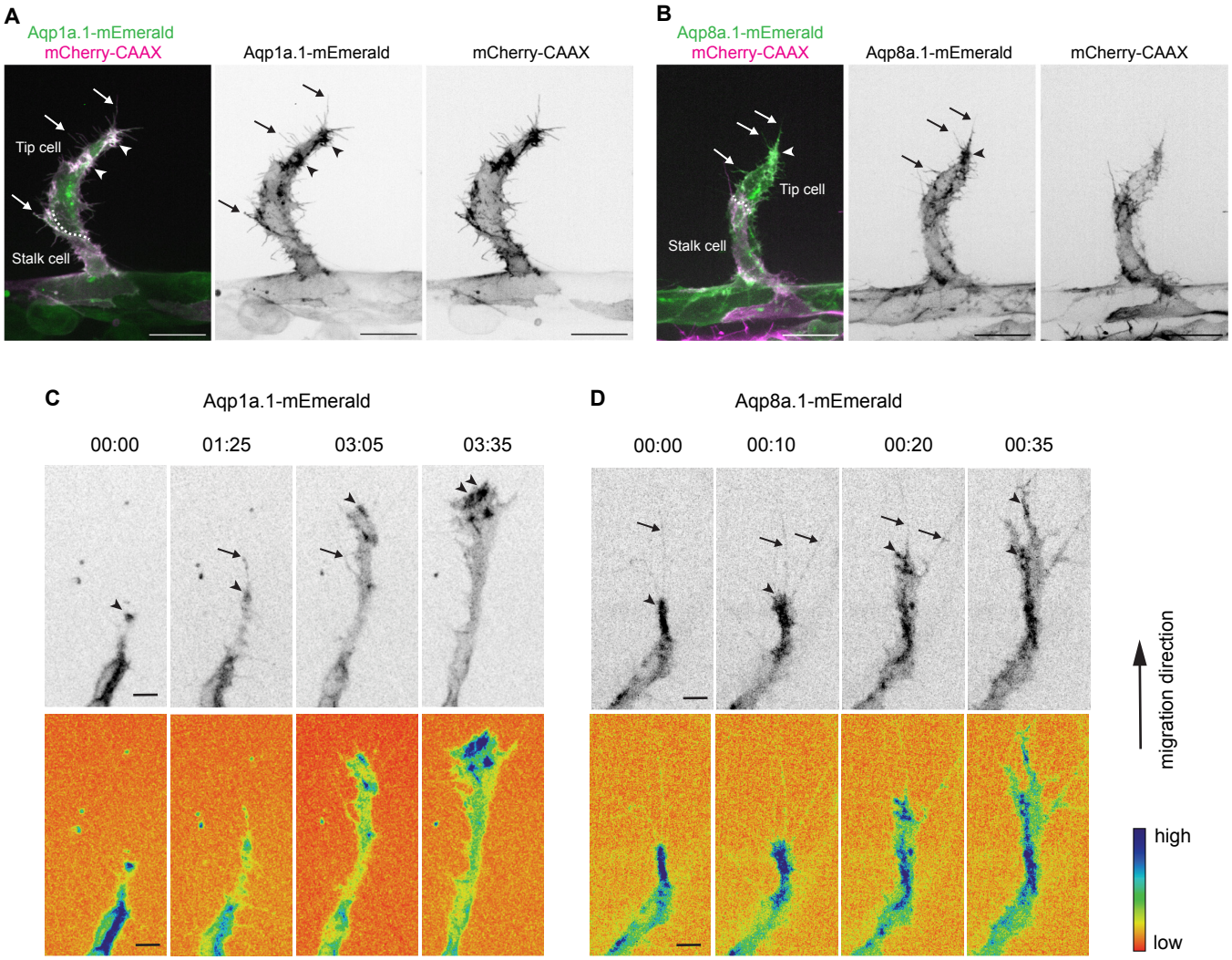
A
Aqp1a.1-mEmerald
mCherry-CAAX
Aqp1a.1-mEmerald
mCherry-CAAX
Tip cell
Stalk cell
B
Aqp8a.1-mEmerald
mCherry-CAAX
Aqp8a.1-mEmerald
mCherry-CAAX
Tip cell
Stalk cell
C
Aqp1a.1-mEmerald
00:00
01:25
03:05
03:35
D
Aqp8a.1-mEmerald
00:00
00:10
00:20
00:35
migration direction
high
low

Figure 3

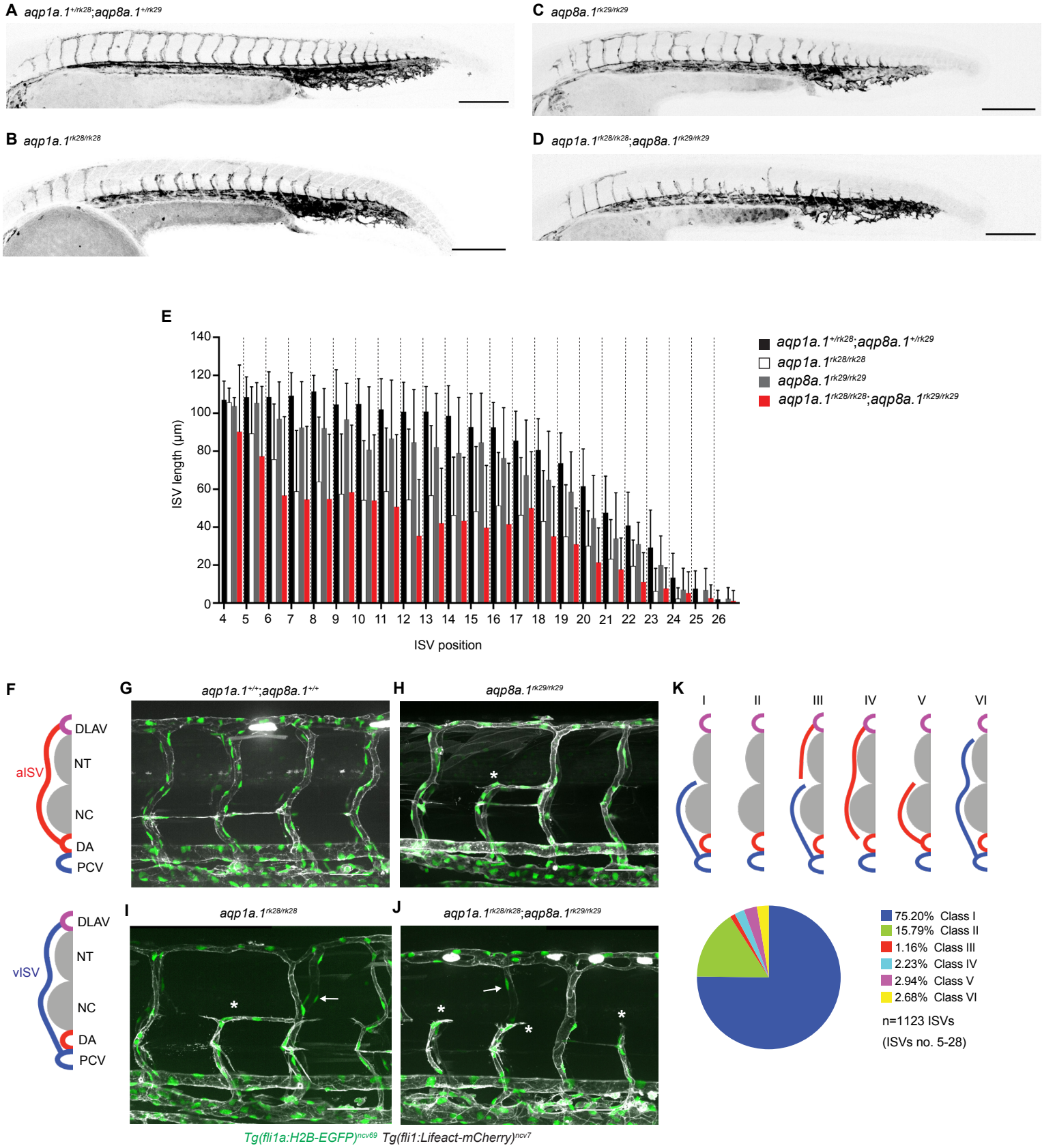
A aqp1a.1+/rk28;aqp8a.1+/rk29
B aqp1a.1rk28/rk28
C aqp8a.1rk29/rk29
D aqp1a.1rk28/rk28;aqp8a.1rk29/rk29
E
ISV length (µm)
ISV position
aqp1a.1+/rk28;aqp8a.1+/rk29
aqp1a.1rk28/rk28
aqp8a.1rk29/rk29
aqp1a.1rk28/rk28;aqp8a.1rk29/rk29
F
DLAV
aISV
NT
NC
DA
PCV
vISV
G aqp1a.1+/+;aqp8a.1+/+
H aqp8a.1rk29/rk29
I aqp1a.1rk28/rk28
J aqp1a.1rk28/rk28;aqp8a.1rk29/rk29
K
I
II
III
IV
V
VI
75.20% Class I
15.79% Class II
1.16% Class III
2.23% Class IV
2.94% Class V
2.68% Class VI
n=1123 ISVs
(ISVs no. 5-28)
Tg(fli1a:H2B-EGFP)ncv69 Tg(fli1:Lifeact-mCherry)ncv7

Figure 4

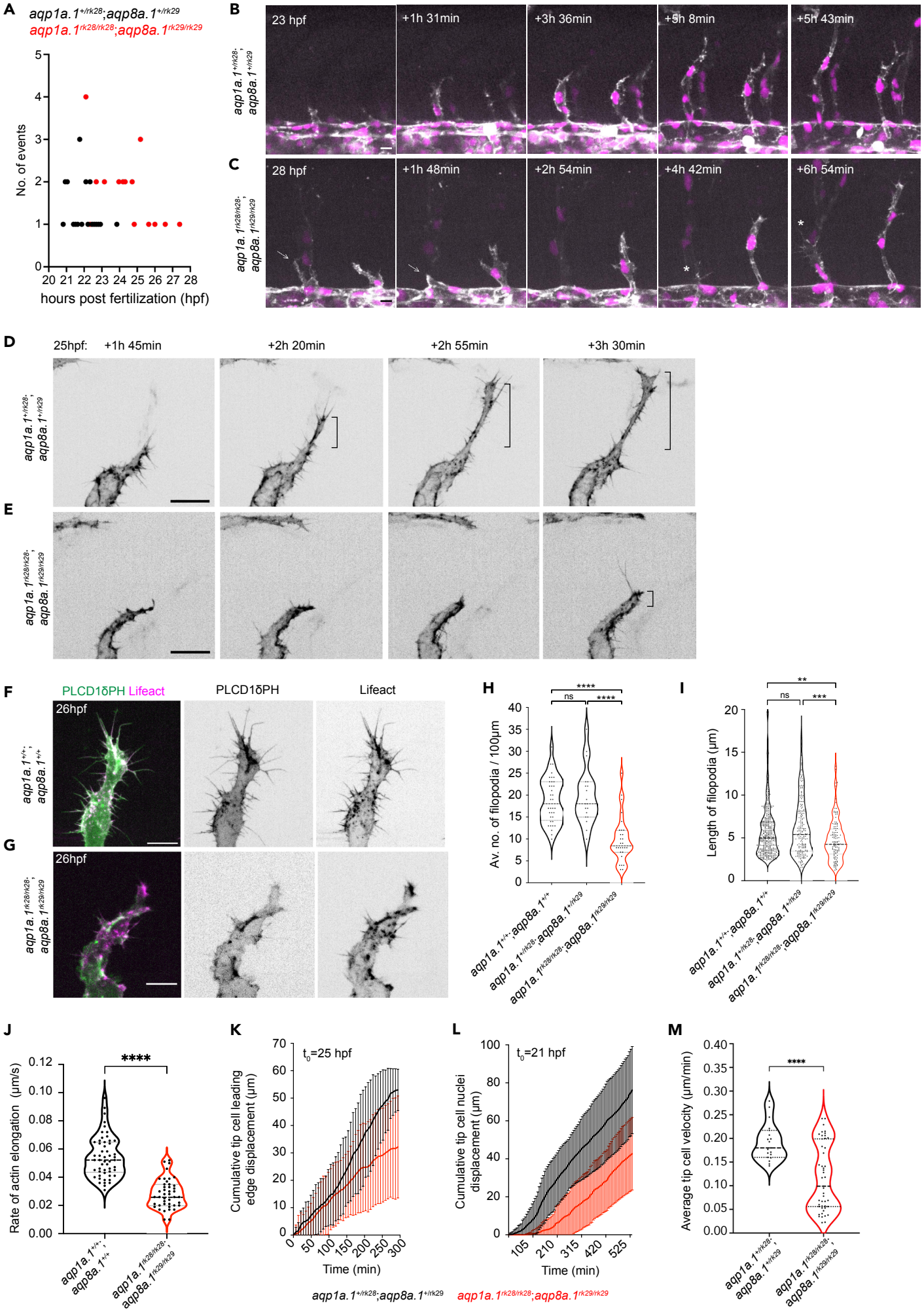
A
aqp1a.1+/rk28;aqp8a.1+/rk29
aqp1a.1rk28/rk28;aqp8a.1rk29/rk29
No. of events
hours post fertilization (hpf)
B
23 hpf
+1h 31min
+3h 36min
+5h 8min
+5h 43min
C
28 hpf
+1h 48min
+2h 54min
+4h 42min
+6h 54min
D
25hpf:
+1h 45min
+2h 20min
+2h 55min
+3h 30min
E
F
PLCD1δPH Lifeact
PLCD1δPH
Lifeact
26hpf
G
26hpf
H
Av. no. of filopodia / 100µm
ns
****
I
Length of filopodia (µm)
ns
**
***
J
Rate of actin elongation (µm/s)
****
K
t0=25 hpf
Cumulative tip cell leading edge displacement (µm)
Time (min)
L
t0=21 hpf
Cumulative tip cell nuclei displacement (µm)
Time (min)
M
Average tip cell velocity (µm/min)
****
aqp1a.1+/rk28;aqp8a.1+/rk29
aqp1a.1rk28/rk28;aqp8a.1rk29/rk29

Figure 5

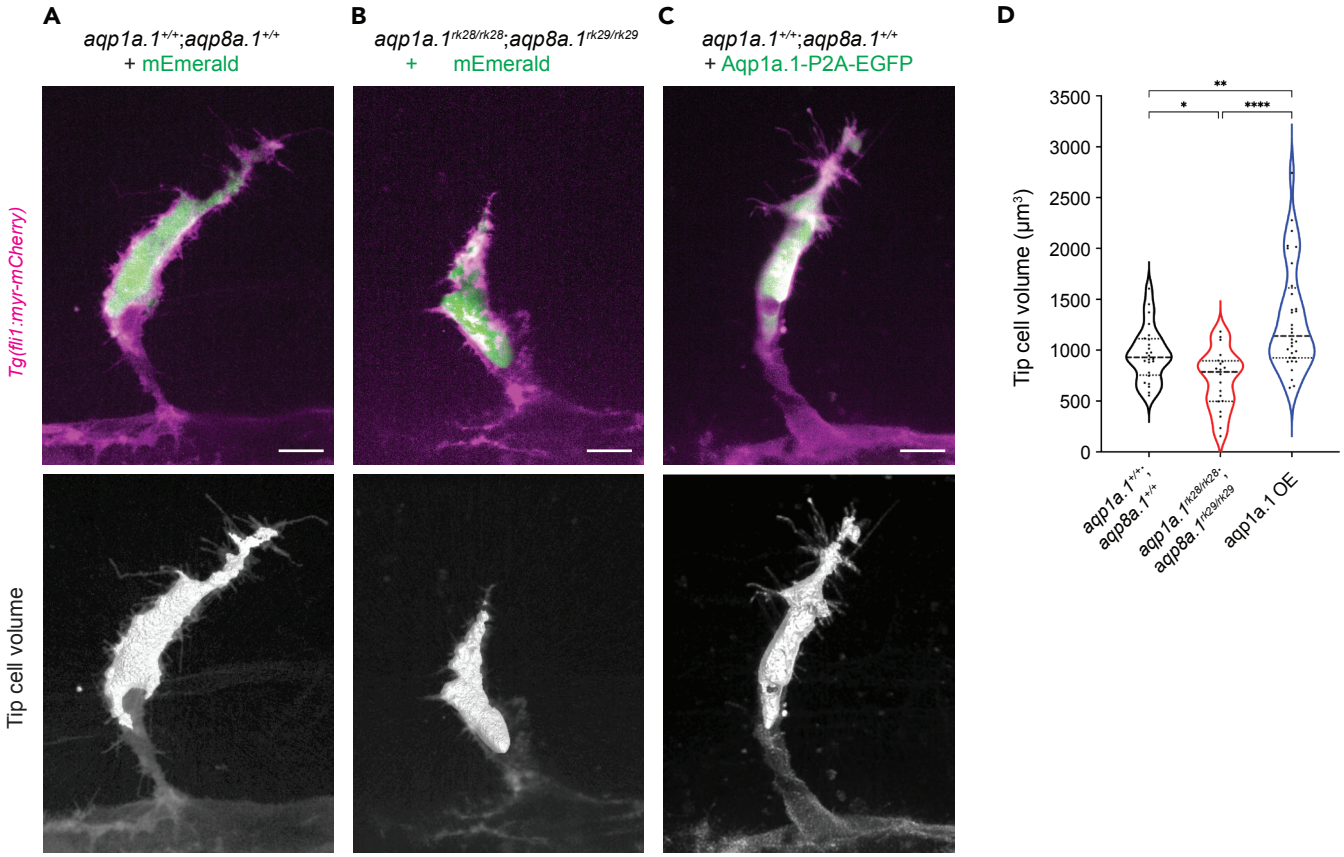
A
aqp1a.1+/+;aqp8a.1+/+
+ mEmerald
B
aqp1a.1rk28/rk28;aqp8a.1rk29/rk29
+ mEmerald
C
aqp1a.1+/+;aqp8a.1+/+
+ Aqp1a.1-P2A-EGFP
D
Tg(fli1:myr-mCherry)
Tip cell volume
Tip cell volume (µm3)
3500
3000
2500
2000
1500
1000
500
0
**
*
****
aqp1a.1+/+; aqp8a.1+/+
aqp1a.1rk28/rk28; aqp8a.1rk29/rk29
aqp1a.1 OE

Figure 6

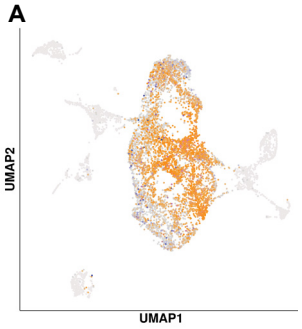

Expression	% of ECs
aqp1a.1 & *lrrc8aa*	12.32
aqp1a.1 only	59.86
lrrc8aa only	2.65
none	25.17

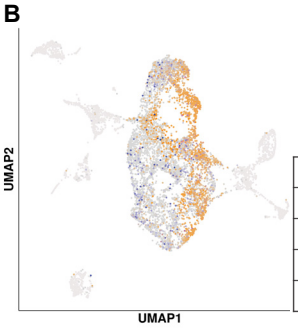

Expression	% of ECs
aqp8a.1 & *lrrc8aa*	10.16
aqp8a.1 only	37.49
lrrc8aa only	4.81
none	47.55

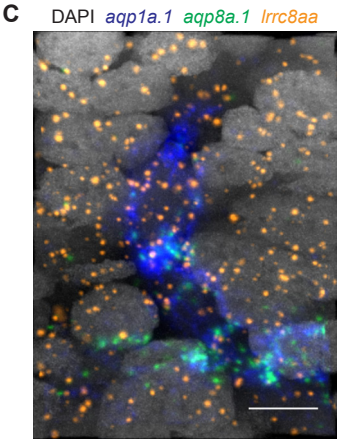

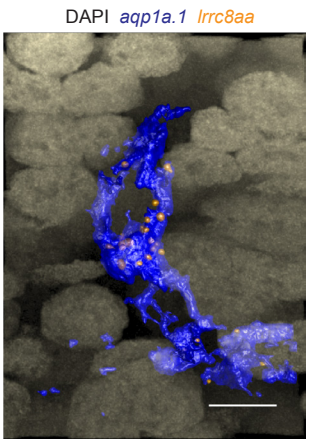

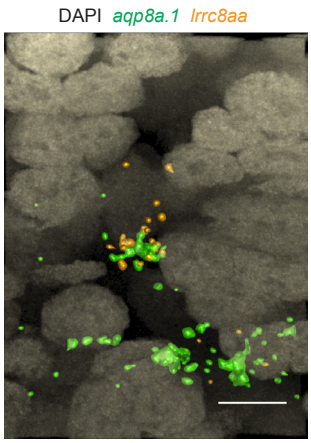

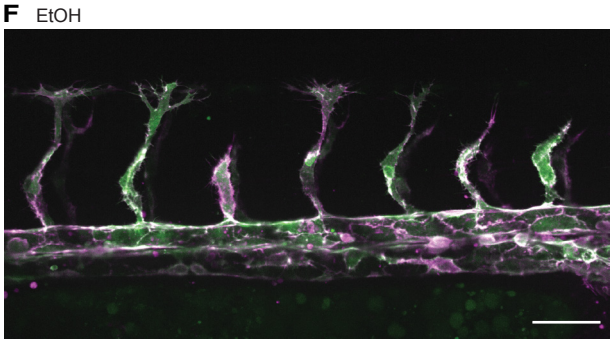

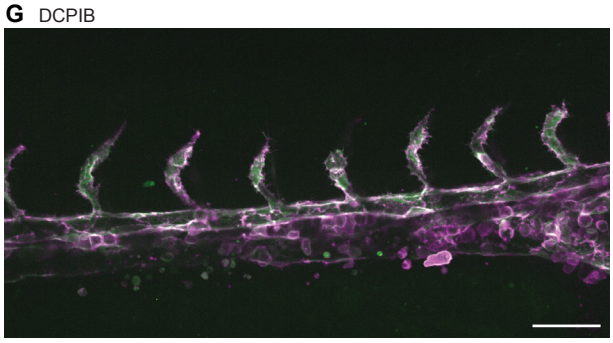

Tg(fli1:Lifeact-mCherry)^{ncv7} Tg(fli1ep:EGFP-PLCδ1PH)^{rk26}

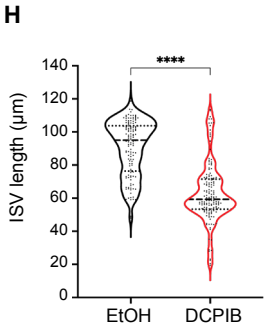

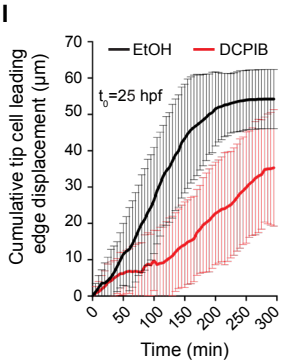

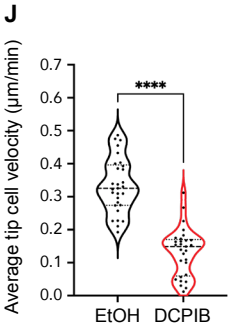

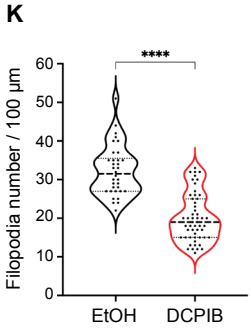

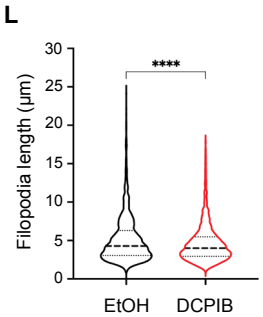

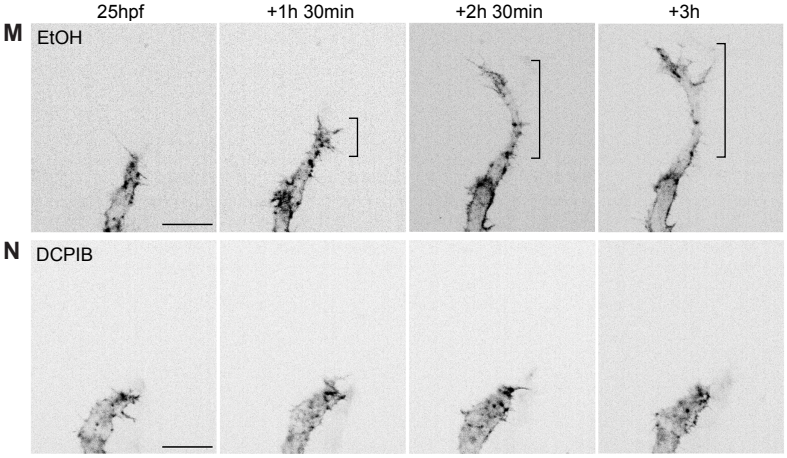

Figure 7

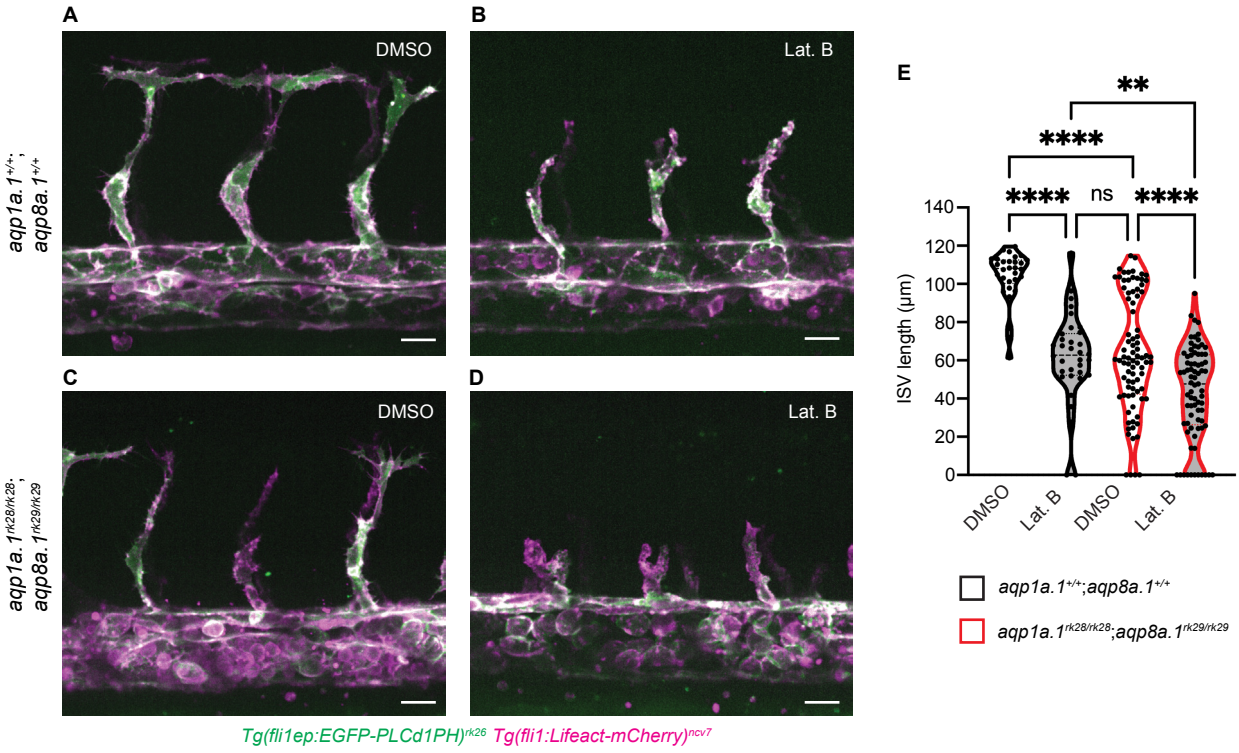
A
B
C
D
E
DMSO
Lat. B
DMSO
Lat. B
aqp1a.1+/+; aqp8a.1+/+
aqp1a.1rk28/rk28; aqp8a.1rk29/rk29
Tg(fli1ep:EGFP-PLCd1PH)rk26 Tg(fli1:Lifeact-mCherry)ncv7
ISV length (µm)
140
120
100
80
60
40
20
0
**
****
****
ns
****
DMSO
Lat. B
DMSO
Lat. B
aqp1a.1+/+;aqp8a.1+/+
aqp1a.1rk28/rk28;aqp8a.1rk29/rk29

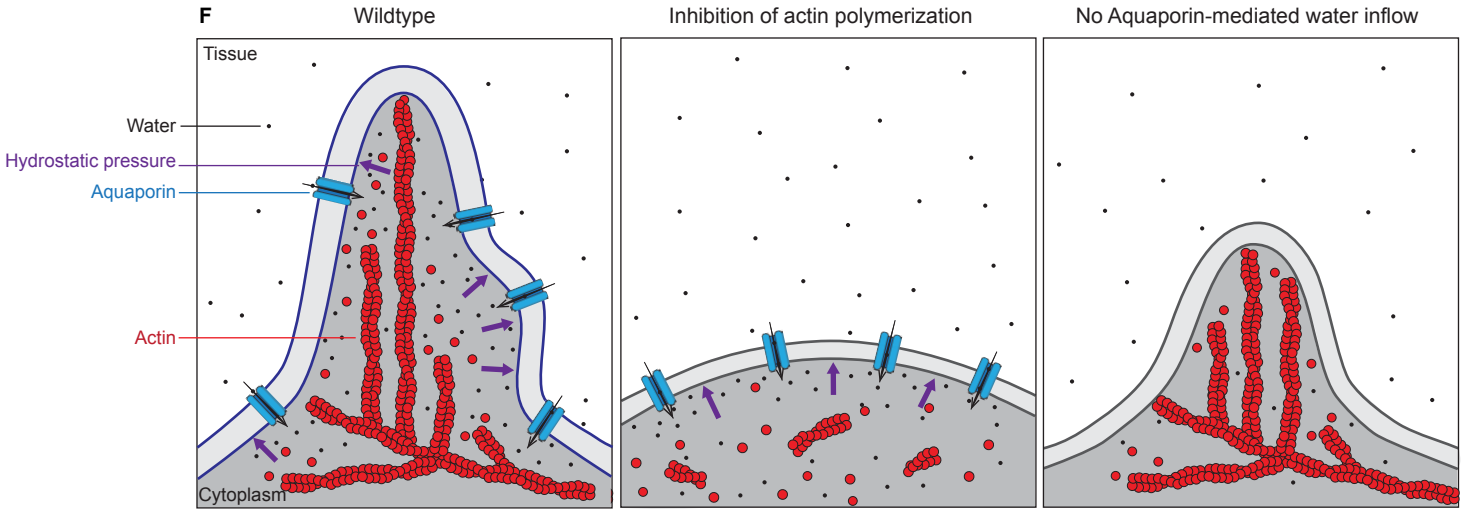
F
Wildtype
Inhibition of actin polymerization
No Aquaporin-mediated water inflow
Tissue
Water
Hydrostatic pressure
Aquaporin
Actin
Cytoplasm
Membrane protrusions generated by actin polymerization and increased hydrostatic pressure.
Membrane protrusions generated by increased hydrostatic pressure.
Membrane protrusions generated by actin polymerization.